Doomed descent? How fast sulphate signals diffuse in the EPICA Dome C ice column

Felix S. L. Ng¹, Rachael H. Rhodes², Tyler J. Fudge³, Eric W. Wolff²

¹School of Geography and Planning, University of Sheffield, Sheffield, UK

²Department of Earth Sciences, University of Cambridge, Cambridge, UK

³Department of Earth and Space Sciences, University of Washington, Seattle, WA, USA

Correspondence to: Felix Ng (f.ng@sheffield.ac.uk)

Abstract. The loss of climate information due to smoothing of ionic impurity signals in ice provides a strong motivation for understanding their diffusion rates at ice-core sites. By analysing sulphate signals in the EPICA Dome C (EDC) core, recent studies estimated the vertical profile of effective diffusivity $D_{\rm eff}$ at that site. However, $D_{\rm eff}$ crudely approximates the local diffusivity D in the ice, it being a nonuniform-weighted average of D over large intervals. We formulate the mathematical inversion for retrieving the D profile from observed signals, which reconciles the findings of the earlier studies as well as elucidating the averaging approximation. Inversion for EDC sulphate reveals a rapid decrease in D through the firn layer – from $\approx 10^{-6} \text{ m}^2 \text{ yr}^{-1}$ at the surface to $\approx 1.7 \times 10^{-8} \text{ m}^2 \text{ yr}^{-1}$ at the firn-ice transition ($\approx 100 \text{ m}$ depth, $\approx 2.5 \text{ ka}$), followed by a gradual decline to $\approx 10^{-10} \, \text{m}^2 \, \text{yr}^{-1}$ through 100–2700 m (2.5–390 ka). This profile enables new interpretation of sulphate transport in the EDC column. We propose vapour diffusion of H₂SO₄ through interconnecting air pores as the cause of the high firm diffusivity. By evaluating the mechanisms controlling D below the firm (diffusion through ice crystals, liquid veins and grain boundaries and diffusion arising from interfacial motion), we infer a dominant partitioning of signals immediately below the firn to a connected vein system, and progressive smoothing of vein signals by Gibbs–Thomson diffusion down to ≈ 2000 m depth, which leaves more and more of the remaining signals to grain boundaries. We conclude that those sulphate signals that survive the initial fast diffusion in the firn to "punch through" to its base might survive into deep ice, and that EDC sulphate preserves a strongly filtered history of volcanic and climatic forcing that underrepresents changes and events shorter than a few years. For the Beyond EPICA – Oldest Ice and Million Year Ice Core drilling sites on Little Dome C, calculations assuming a diffusivity profile like our EDC profile and not exceeding $10^{-10} \,\mathrm{m^2 \ yr^{-1}}$ in ice older than 450 ka constrain the sulphate diffusion length in ice 1–2 Ma old to 2 cm at most, and probably as low as ≈ 1 cm, for atmospheric-sourced signals that experienced only diffusion and mechanical shortening in the column.

1 Introduction

45

60

Ionic impurities in ice cores provide valuable records of climate and environmental change (e.g. Legrand and Mayewski, 1997). The realisation that impurity signals in ice may be altered – not necessarily carrying climatic information "written in stone" – motivates study of the post-depositional processes threatening their integrity. Diffusion attenuates and broadens signals as they descend the ice column, potentially causing severe signal loss at depth, where the diffusion rate may be enhanced by higher temperature. The vertical pattern of the diffusion rate is of interest to questions about the reliability of ice-core ion records, the amount of climatic information retrievable from their signals, and the methods of reconstructing past forcings at the ice-sheet surface – questions that matter the more as ice-coring campaigns seek older and older records, such as in the Beyond EPICA – Oldest Ice project (BE-OI, 2017) and Million Year Ice Core project (MYIC, 2020).

Recently, Fudge et al. (2024) and Rhodes et al. (2024) quantified diffusion on the high-resolution sulphate record of the EPICA (European Project for Ice Drilling in Antarctica) Dome C or "EDC" ice core (EPICA community members, 2004) from Antarctica. This record of sulphate concentration, measured by fast-ion chromatography (FIC) on bulk ice samples at \approx 4 cm spacing down to 770 m depth and 1–2 cm spacing at greater depths (Traversi et al., 2002, 2009), is shown in Fig. 1a. By analysing how its signals vary along the core, together with a signal-evolution model that accounts for diffusion and vertical mechanical shortening of the ice, Fudge et al. (2024) and Rhodes et al. (2024) estimated the "effective diffusivity" $D_{\rm eff}$ of sulphate at EDC.

Sulphate is relevant in the diffusion context because volcanic events, which occur as sharp peaks on such records, provide data for synchronising ice-core timescales (e.g., Severi et al., 2012; Svensson et al., 2020) and inferring the history of volcanism – the record in Fig. 1a has been used to study eruption frequency back as far as 200 ka (Castellano et al., 2004; Lin et al., 2022; Wolff et al., 2023). Sulphate may also experience rapid transport in the liquid veins of polycrystalline ice, given the low eutectic temperature of sulphuric acid (-73°C) implies its likely dissolution in vein water located at grain triple junctions (Mulvaney et al., 1988; Wolff et al., 1988; Nye, 1989; Mader, 1992), and given theoretical modelling which shows that ionic signals residing in a network of connected veins diffuse rapidly due to the Gibbs–Thomson effect (Ng, 2021). However, when studying impurity transport in ice, it is difficult to know how the bulk concentration of an ion partitions into contributions from different impurity sites – the ice-crystal lattice, grain boundaries, veins, and micro-inclusions; the mechanisms of impurity transfer between these sites also remain elusive (Barnes et al., 2003; Ng, 2021; Stoll et al., 2021). Thus, our understanding of how signals on the bulk concentration evolve is incomplete. Because the model used by Fudge et al. (2024) and Rhodes et al. (2024) in their diffusivity inversions tracks sulphate bulk concentration without resolving the partitioning, their effective diffusivities (D_{eff}) estimates for the EDC site reflect the overall outcome of different grain-scale transport processes. Yet, for this reason, their estimates provide global constraints on how these processes operate.

In this paper, we formulate a theory of diffusivity inversion that extends the methods of Fudge et al. (2024) and Rhodes et al. (2024), and which may be applied to other ions and to other ice cores besides EDC. Their studies referred to the "effective diffusivity" in part because of the caveat about impurity partitioning, but more specifically because their inversions assumed

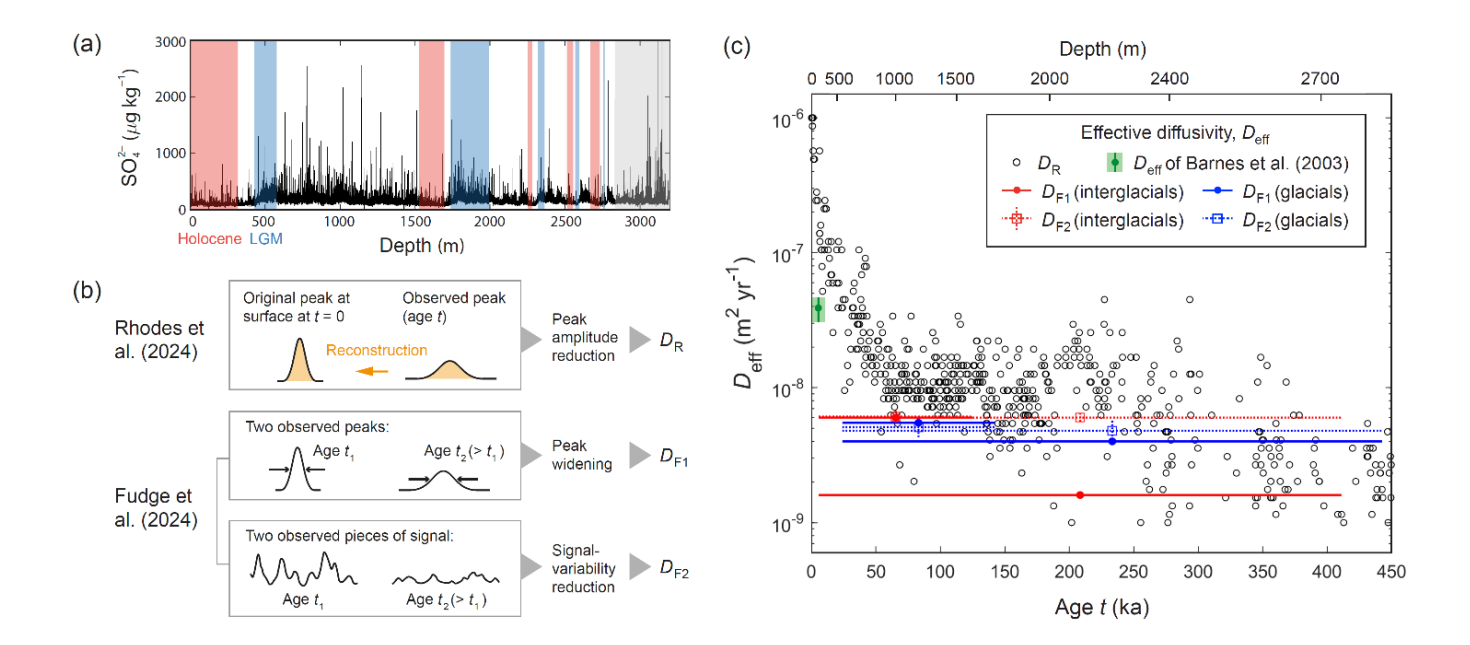


Figure 1. Approaches and results of the inversions for effective diffusivity *D*_{eff} by Fudge et al. (2024) and Rhodes et al. (2024), for sulphate at the EPICA Dome C ice-core site. (a) Depth profile of sulphate concentration from fast ion chromatography (Traversi et al., 2009), showing abundant peaks, many of them recording volcanic eruptions. Interglacial and glacial maximum periods are highlighted by red and blue shading, respectively; for their age and depth ranges, see Table A1 of Fudge et al. (2024). Grey shading marks the record > 2800 m, which is not studied herein. (b) Schematic of the approaches of Rhodes et al. (2024) and Fudge et al. (2024) for finding their *D*_{eff} estimates – *D*_R, *D*_{F1}, and *D*_{F2} which are based on peak-amplitude decay, peak widening and signal-variability reduction, respectively. (c) Plot of their *D*_R, *D*_{F1}, and *D*_{F2} results versus age back to 450 ka. The depth scale is indicated on the top axis. Horizontal bar shows the age range of each *D*_{eff} estimate, and vertical bar its uncertainty. Green point plots the *D*_{eff} estimate of Barnes et al. (2003) for the Holocene part of the record.

constant diffusivity acting on each signal as it evolves. Accordingly, they recognised $D_{\rm eff}$ as some weighted average of the true diffusivity. The averaging process has not been made clear though. We show mathematically that their $D_{\rm eff}$ estimates, owing to the averaging approximation, deviate significantly from the true diffusivity D (unless noted otherwise, all diffusivities in this paper pertain to sulphate). We improve upon their results to obtain the vertical profile of D in the EDC ice column, deriving new information about ionic impurity transport there. Notably, we discover high D values localised to the firn layer, whose cause is discussed towards the end. We also briefly consider what the findings mean for signal survivability at the sites of the BE-OI and MYIC projects. For convenience, we abbreviate Fudge et al. (2024) and Rhodes et al. (2024) as "F2024" and "R2024", respectively, given how often they are referenced below.

Figure 1 illustrates their diffusivity inversions. R2024's approach utilised the decay of signal peak amplitude, whereas F2024 employed two approaches, one based on signal peak widening and the other on the decay of signal variability down

core (Fig. 1b). In R2024, 537 sulphate peaks were identified in the record down to \approx 2800 m depth (0–450 ka). For each peak, the height of the corresponding original peak at deposition on the ice-sheet surface is reconstructed, by assuming that it held the same amount of sulphate as the observed peak (after removing local background concentration due to non-volcanic sources of sulphate such as marine biogenic emissions) and that it was Gaussian-shaped, with a duration of 3 years at "full width at tenth maximum" (FWTM), as is typically found for the width of volcanic sulphate peaks in Antarctica snow; see R2024 for detailed justification. Then, using their model, which we give in Eq. (1) below, R2024 numerically simulated the evolution of the reconstructed peak forward in time, tuning the diffusivity in multiple model runs to match the observed peak's height at its recorded age, to find D_{eff} for the peak. We denote by D_{R} their amplitude-based D_{eff} estimate.

90

100

105

In contrast, F2024 studied only signals in interglacial and glacial maximum periods (red and blue shading in Fig. 1a) and made separate inversions for these period types, to cater for the possibility of interglacial ice and glacial ice having different diffusivities. This is motivated by the idea that the different ice-column conditions (e.g. strain rate, mean crystal size) in these periods might affect impurity transport differently. Their width-based inversion, which gauges each peak's width by its "full width at half maximum" (FWHM), performs best-fit numerical simulations as R2024 did, but uses two peaks below the surface (Fig. 1b) rather than one peak and its reconstructed surface counterpart. Specifically, for interglacials and glacial maxima separately, they ran simulations to evolve a Gaussian signal with an initial width equal to the median width of observed peaks in the earlier interglacials or glacial maxima, thus backing out D_{eff} for the intervening intervals. We denote by D_{FI} their width-based D_{eff} estimate.

The other approach of F2024 uses a method pioneered by Barnes et al. (2003) for quantifying signal variations in terms of "mean absolute gradient" (explained in Sect. 2.3) to estimate $D_{\rm eff}$ from the decrease of signal variability down core. Using the method, Barnes et al. (2003) had estimated $D_{\rm eff} = 3.9 \pm 0.8 \times 10^{-8} \,\mathrm{m^2\,yr^{-1}}$ for the Holocene part (top 350 m) of the sulphate record in Fig. 1a. F2024 essentially applied the method to older parts of the core, focusing on the sequence of interglacials and glacial maxima. We denote by $D_{\rm F2}$ their gradient-based $D_{\rm eff}$ estimate (Fig. 1b).

The effective diffusivities of R2024 and F2024 (Fig. 1c) show striking differences. Although D_R , D_{F1} and D_{F2} in the deeper record ≈ 200 to 450 ka (≈ 2100 –2800 m) have similar magnitudes, $\sim 10^{-9}$ – 10^{-8} m² yr⁻¹, D_R is much higher (up to 10^{-6} m² yr⁻¹) than D_{F1} and D_{F2} in ice $\lesssim 50$ ka, where it decays with age and depth. As R2024 reported, their median D_R value for Holocene ice (0–10 ka), 2.4×10^{-7} m² yr⁻¹, is nearly ten times the D_{eff} estimate of Barnes et al. (2003) (green data point in Fig. 1c). Beyond its initial decay, D_R averages at $\approx 10^{-8}$ m² yr⁻¹ in 50–200 ka, still about twice that of D_{F1} and D_{F2} . On seeing that D_{F1} and D_{F2} ($\approx 5 \times 10^{-9}$ m² yr⁻¹) are not much higher than the self-diffusivity of ice ($\approx 3 \times 10^{-10}$ to 3×10^{-9} m² yr⁻¹ at –50 to –35°C; Ramseier, 1967), F2024 inferred that the fast signal diffusion in liquid veins modelled by Ng (2021) occurs only to a limited extent for sulphate in the upper $\approx 90\%$ of the ice column, and hence most sulphate there resides within ice crystals and at grain boundaries – not in the veins. On the other hand, R2024 interpreted the initial high (falling) D_R values for significant (diminishing) diffusion of sulphate in interconnected veins in the top quarter of the ice column.

Resolving these differences is imperative because the diffusivity profile is key to understanding how the crystal-scale diffusion mechanisms vary with depth and the factors involved, such as impurity partitioning. Besides adopting different inversion approaches, R2024 and F2024 processed the FIC data differently. R2024 only analysed sulphate peaks that are certainly volcanic by omitting others coincident with dust peaks, whereas F2024 applied the scaling procedure of Barnes et al. (2003) to the sulphate record to reduce the influence of background climate variations before extracting signals for analysis. These methodological differences can only explain minor discrepancies, not the overall incompatibility, between D_R and $D_{F1,2}$. The results in Fig. 1c also raise intriguing questions, notably the cause of the near-surface decay in D_R in ≈ 0 –50 ka, which seems to continue through ≈ 100 –450 ka at lower rate, and why (as both their studies pointed out) D_{eff} does not increase with depth, against the expectation that molecular diffusivity increases with temperature. The ice temperature at the EDC site increases monotonically from $\approx -53\,^{\circ}\text{C}$ at the surface to $\approx -12\,^{\circ}\text{C}$ at 2800 m (Fig. S1 in the Supplement).

Herein, our theory not only allows estimating the true diffusivity D, which is a more fundamental quantity than D_{eff} for probing impurity transport mechanisms; it also shows how the D_R , D_{F1} and D_{F2} estimates may be reconciled on account of their underlying averaging and two needed corrections in the D_{F2} inversion. A key insight is that the signal-evolution model of F2024 and R2024 can be solved analytically, so the inversions can be done without numerical simulation. While our inversion results draw interest to the firn diffusivity, their signal-evolution model ignores firn densification; we therefore also examine its validity when used for inversions within the firn.

We focus on the EDC record in 0–2800 m (Fig. 1) by using the data collected by R2024 and F2024 without reprocessing the FIC sulphate concentrations. The record at depths > 2800 m (which features in part of F2024's study) is excluded for the reason given by R2024: there, some sulphate peaks may be non-volcanic and shaped by post-depositional processes other than diffusion and vertical mechanical shortening. This is shown by the presence of (i) anomalous peaks below 2800 m depth that have been chemically modified, as evidenced by ion association (Traversi et al., 2009), and (ii) other anomalous peaks starting from ≈ 2700 m (perhaps as shallow as 2500 m) that exhibit side troughs, indicating sulphate being "sucked" from neighbouring background levels towards zones with high cation concentration to form the peaks (Wolff et al., 2023). These artefacts reflect added complexity in the evolution of signals in deep ice at EDC that makes their origin uncertain. Our theory and analyses strictly concern signals without such artefacts, which give the ideal input data for inversion. While R2024's data mitigate the issue by excluding potential artefact peaks during data collection, the deepest data of F2024 used by us may contain artefact signals, especially anomalous peaks of type (ii); but, for reasons explained later, this should not affect our conclusions.

2 Mathematical theory

2.1 Signal evolution

115

120

125

130

135

140

145

We begin with the advection–diffusion equation for signal evolution down the ice column, used by F2024 and R2024. In a coordinate frame moving with the ice, where z denotes distance below a material horizon descending towards the bed, signals in the bulk impurity concentration C(z, t) (measured in $\mu g kg^{-1}$, or $\mu g L^{-1}$ of meltwater) evolve according to

$$\frac{\partial C}{\partial t} = D(t) \frac{\partial^2 C}{\partial z^2} - \dot{\varepsilon}_z(t) z \frac{\partial C}{\partial z}.$$
 (1)

Here, t is the age of the horizon, D is the impurity diffusivity, and $\dot{\varepsilon}_z$ (< 0) is local vertical strain rate. Eq. (1) encapsulates the effects of mechanical shortening and diffusional spreading. Table A1 lists other mathematical symbols used in the paper.

Following F2024 and R2024, we use Eq. (1) to model sulphate signals, assuming an invariant strain-rate profile and constant surface accumulation rate at the core site – thus, a steady-state column with constant thickness and vertical velocity profile. In this system, signals travel through fields that are functions of depth in the column only, not time, so the age–depth scale allows translation between D(t) and its vertical profile. Material at age t has shortened from its original thickness at the surface by the thinning factor S, given by

155
$$S(t) = \exp \int_0^t \dot{\varepsilon}_z(\eta) \, d\eta$$
, (2)

where η denotes the variable of integration. Differentiating Eq. (2) gives $dS/dt = \dot{\varepsilon}_z S$. The thinning function S decays with age t from its value at the surface, $S_0 = S(t=0) = 1$.

The inversion methods of R2024 and F2024 (elaborated in Sects. 2.2 and 2.3) use Eq. (1) as the basis, but as noted earlier, assume a constant D for each signal as it evolves down column. The resulting effective diffusivities D_R , D_{F1} and D_{F2} do not strictly represent the true (local) diffusivity D, instead averages measuring its cumulative effect over finite age and depth intervals; as we shall see, these intervals are large. By solving Eq. (1) analytically below, we develop exact inversions for D(t) that circumvent this assumption, at the same time deriving equations linking D(t) to D_R , D_{F1} and D_{F2} . How Eq. (1) is affected by firn densification will be examined in Sect. 3.5, after we glimpse high firn diffusivity from our inversions.

2.2 Theory: peak-based inversions

2.2.1 The inversion possibility

150

160

165

170

A key property we exploit is that a Gaussian signal stays Gaussian under the combined mechanical shortening and diffusional spreading described by Eq. (1). F2024 and R2024 both initialised their simulations with Gaussian peaks, but did not harness this property. As alluded to by R2024, the sulphate flux from eruptions reaching the ice sheet often varies asymmetrically in time, but the deposited peaks rapidly relax to near-Gaussian. This motivates a Gaussian approximation to their shape.

To see the property, define the transformed depth

$$\zeta = \frac{z}{S(t)} \tag{3}$$

and define the variable

$$\tau(t) = \int_0^t \frac{D(\eta)}{S^2(\eta)} d\eta + \tau_0, \tag{4}$$

where τ_0 is the value of τ at zero age. Here, ζ is the destrained or unthinned thickness, and τ , an indirect proxy of age or time, accounts for the histories of diffusion and layer thinning. On letting $C(z, t) = f(\zeta, \tau)$, these changes of variable convert Eq. (1) to the classical heat equation

$$\frac{\partial f}{\partial \tau} = \frac{\partial^2 f}{\partial \zeta^2} \,, \tag{5}$$

which has the well-known (Gaussian) similarity solution

190

195

$$f(\zeta, \tau) \propto \frac{1}{\sqrt{\tau}} e^{-\zeta^2/4\tau} \,. \tag{6}$$

In the ζ -direction, this Gaussian's width expressed as a standard deviation is $\sigma = (2\tau)^{1/2}$. Eqs. (5) and (6) mean that in $\tau - \zeta$ space, signals experience uniform diffusion at unit rate, and a Gaussian peak decays in amplitude following the factor $1/\sqrt{\tau}$ and widens following $\sqrt{\tau}$. Consequently, observations of peak widening or amplitude reduction down core, which provide data on $\tau(t)$, can be used to recover D(t) via Eq. (4). This idea forms the basis of the peak-based inversions.

For example, consider an amplitude-based inversion, where the "relative peak amplitude" (the ratio of a peak's observed amplitude to its original amplitude on deposition at the surface at t = 0) has been compiled for different peaks along the core, as done by R2024. Suppose the relative amplitudes vary with age to trace out the function $\alpha(t)$. Then we have $\alpha(t) = \sqrt{\tau_0/\tau}$ according to Eq. (6), and differentiating Eq. (4) with respect to t gives the inversion

$$D(t) = S^{2}(t)\frac{d\tau}{dt} = S^{2}\frac{d}{dt}\left(\frac{\tau_{0}}{\alpha^{2}}\right) = -\frac{2\tau_{0}S^{2}\alpha'}{\alpha^{3}}$$

$$\tag{7}$$

(the ' denotes derivative). This inversion requires the value $\tau_0 = \tau(t=0)$. For each observed peak, R2024 reconstructed the amplitude of the original peak by assuming it to be Gaussian, with a 3-year duration at FWTM and carrying the same total impurity load as the observed peak. They ignored firn densification effects and used the ice density in the reconstruction. We therefore set $\tau_0 = \sigma^2/2$, with $\sigma = 3$ yr × a/4.2919, where σ (m) is the standard deviation mentioned above, and a is the ice-equivalent accumulation rate (m/yr), and the factor 4.2919 converts the FWTM of the Gaussian to σ . Positive τ_0 ensures a finite amplitude for the initial peak in Eq. (6). The differentiation in Eq. (7) assumes α to be smoothly varying; in practice, one fits a curve to the α -data prior to inversion.

Similarly, in a width-based inversion, where data on "relative peak width" (the ratio of observed width to original width) trace out the function $\beta(t)$, such that $\beta(t) = \sqrt{\tau(t)S^2(t)/\tau_0S_0^2} = S(t)\sqrt{\tau(t)/\tau_0}$, we derive

$$D(t) = S^{2}(t)\frac{d\tau}{dt} = S^{2}\frac{d}{dt}\left(\frac{\tau_{0}\beta^{2}}{S^{2}}\right) = 2\tau_{0}\beta(\beta' - \beta\dot{\varepsilon}_{z}).$$
(8)

Applying this inversion necessitates an assumption for the original peak width (for compiling β and τ_0). However, for comparing against the width-based inversion of F2024, Eq. (8) first needs to be adapted for use on two peaks below the surface, rather than one at the surface and one below (Fig. 1b). We attain the relevant result via a different route below.

2.2.2 Full-fledged theory

Before applying the above theory to data, we expand the mathematical analysis to unravel how peak-based inversions work and establish the relationship between D(t) and the effective diffusivities of F2024 and R2024.

The ratio D/S^2 recurring in Eqs. (4), (7) and (8) relates a physical effect. As a signal shortens mechanically, its variations steepen, so it diffuses faster than if shortening were absent. With S < 1 below the surface, D/S^2 represents the amplified diffusivity. Another way of picturing this effect is to imagine the signal experiencing the diffusivity D, but over a longer time – longer by $1/S^2$ times. This motivates us to introduce another age variable, ψ , defined by $d\psi = dt/S^2(t)$. Specifically, we set $\psi = 0$ at t = 0, so that

210
$$\psi(t) = \int_0^t S^{-2}(\eta) \, d\eta$$
 (9)

This function has unit slope at t = 0 (since S(t = 0) = 1) and curves upward (e.g. Fig. 3c). We call ψ the *dilated age* because it accounts for thinning but excludes diffusion, unlike the proxy variable τ , which accounts for both.

On moving from t–z to ψ – ζ space (Fig. 2), the transformation z to ζ geometrically destrains the signal to track material horizons, whereas the transformation t to ψ stretches time to capture the mechanically-induced enhanced diffusion on the signal. With coordinate stretching absorbing both effects, the transformed signal obeys $\partial C/\partial \psi = D(\psi)\partial^2 C/\partial \zeta^2$ without a shortening term (Fig. 2b). Crucially, under the move, Eq. (4) is converted to

$$\tau(\psi) = \int_0^{\psi} D(\psi) d\psi + \tau_0, \tag{10}$$

which shows that inversion for D fundamentally involves

$$D(\psi) = \frac{d\tau}{d\psi} \,. \tag{11}$$

220 In other words, as a Gaussian peak evolves in ψ - ζ space, its unthinned width squared and its inverse squared amplitude (recall

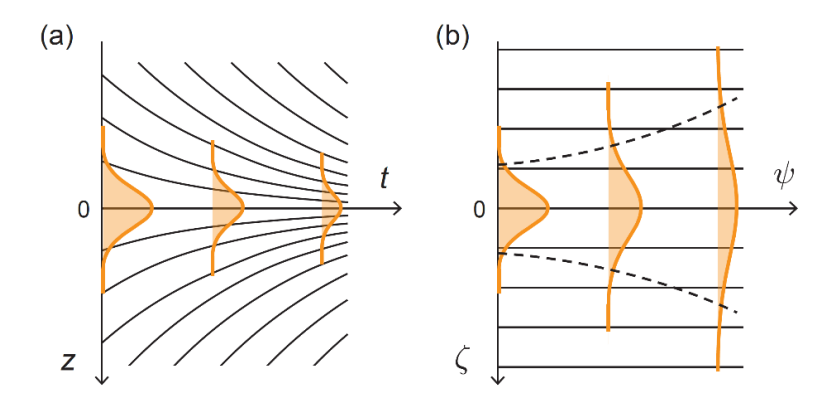


Figure 2. Evolution of a Gaussian signal in (a) t–z space and (b) ψ – ζ space. Solid black curves signify material trajectories. Dashed curve in (b) marks the unthinned signal width, whose square increases at a rate with respect to ψ that reflects the instantaneous diffusivity.

that unthinned width $\propto \sqrt{\tau}$ and amplitude $\propto 1/\sqrt{\tau}$) increase at a rate with respect to ψ that equals the instantaneous or local diffusivity. Equivalently, the local diffusivity is given by the rate of change of these peak-form parameters with respect to dilated age ψ (Fig. 2b). Not surprisingly, the age-domain inversions in Eqs. (7) and (8) also involve rates of change.

Given these insights, we can calculate the effective diffusivities D_R and D_{F1} of R2024 and F2024 analytically, which obviates need to integrate Eq. (1) numerically and perform multiple simulations to fit data. As noted before, their inversions assumed constant D during each signal's descent. If Eq. (10) is used to reproduce their inversions, then we set $D \equiv D_{eff}$ (constant) in its integral, which gives

$$\tau(\psi) = D_{\text{eff}} \psi + \tau_0, \tag{12}$$

or

230

$$D_{\text{eff}} = \frac{\tau - \tau_0}{\psi} = \frac{\tau_0}{\psi} \left(\frac{\tau}{\tau_0} - 1 \right),\tag{13}$$

which describes the inversion based on a subsurface peak and its reconstructed original (surface) peak. Where the inversion uses a pair of subsurface points, say, τ_1 at dilated age ψ_1 and τ_2 at dilated age ψ_2 , differencing the application of Eq. (12) to these data yields

$$D_{\rm eff} = \frac{\tau_2 - \tau_1}{\psi_2 - \psi_1}. (14)$$

From these results, it follows that the R2024 inversion is equivalent to

$$D_{\mathbf{R}}(t) = \frac{\tau_0}{\psi(t)} \left(\frac{1}{\alpha^2(t)} - 1 \right),\tag{15}$$

with ψ given by Eq. (9) and the data for α and τ_0 gathered as before (Sect. 2.2.1), whereas the width-based inversion of F2024 for two peaks of age t_1 and t_2 has the analytical counterpart

$$D_{\rm Fl} = \frac{\tau(t_2) - \tau(t_1)}{\psi(t_2) - \psi(t_1)},\tag{16}$$

in which the τ values derive from observed peak widths. F2024 measured the unthinned FWHM of each peak, so $\tau = \sigma^{*2}/2$, where $\sigma^* = \text{FWHM}/2.3548$ is the destrained standard deviation of the Gaussian.

The effective diffusivity from Eq. (15) or (16) is valid for the specific interval bracketed by the paired data, as in R2024 and F2024's simulation-based inversions. The interval in R2024's inversion spans each peak's entire history. In F2024's inversion, which uses paired data between the Holocene and earlier interglacials or between the LGM and earlier glacial maxima, the intervals exceed ~ 100 kyr. Thus, D_R of R2024 and D_{F1} of F2024 are effective diffusivity estimates for different periods – this is a key reason behind their discrepancy, which we will point out again when analysing results in Sect. 3.

Next we relate the effective diffusivities to the true diffusivity D(t). Applying Eq. (10) to paired data (ψ_1, τ_1) and (ψ_2, τ_2) , eliminating τ_0 , and using Eq. (14), yields

$$D_{\text{eff}} = \frac{1}{\psi_2 - \psi_1} \int_{\psi_1}^{\psi_2} D(\psi) d\psi, \qquad (17)$$

OI

$$D_{\text{eff}}(\psi) = \frac{1}{\psi} \int_0^{\psi} D(\psi) d\psi \tag{18}$$

if the upper data point lies at the surface. These results show that D_{eff} is the interval average of D, not over t but over the dilated age ψ . Since $\psi(t)$ curves upward (Fig. 3c), D_{eff} is biased towards D in the older part of the averaging interval; but it is influenced by D in the younger part. The larger is the interval, the more crudely D_{eff} approximates D at the lower (deeper) data point. Equation (18) leads to further insights on the profile $D_{R}(t)$ retrieved by the R2024 inversion. By evaluating its integral,

260
$$D_{\rm R}(t) = \frac{1}{\psi(t)} \int_0^t D(\eta) \psi'(\eta) \, d\eta = D(t) - \frac{1}{\psi(t)} \int_0^t D'(\eta) \psi(\eta) \, d\eta$$
. (19)

working with time rather than ψ as the integration variable, we derive

According to this expression, D_R found from an observed peak not only reflects the local diffusivity D at its depth, but also inherits a signal from the variations in D throughout its earlier shallower history: we call this the "memory effect". Notably, $D_R(t)$ overestimates (underestimates) D(t) if D(t) is a decreasing (increasing) function.

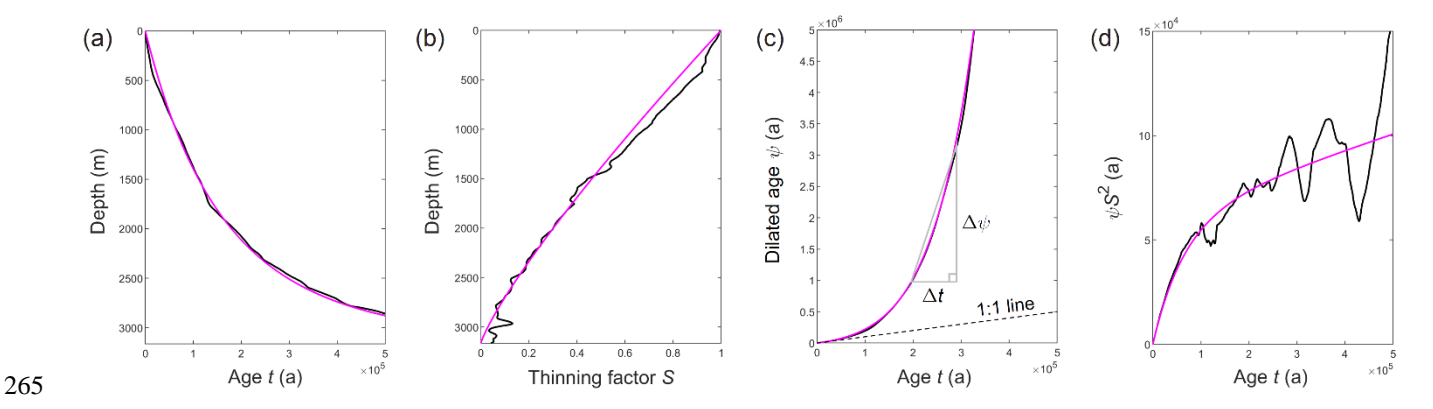


Figure 3. Functions used in our diffusivity inversions for the EPICA Dome C ice-core site: (a) the AICC2012 age—depth scale (Bazin et al., 2013; Veres et al., 2013) and the corresponding (b) depth profile of thinning factor S, (c) dilated age ψ versus age t, and (d) ψS^2 versus age. Black curves derive directly from the AICC2012 scale. Magenta curves, used in our inversions, are smooth approximations based on an ice-flow model assuming the submergence velocity $w_i = a_s(h/H)^{1.2}$, where h is height above the bed, H = 3165 m (mean ice thickness chosen by Rhodes et al., 2024), and surface accumulation rate $a_s = 0.0195$ m yr⁻¹. Grey triangle in (c) illustrates the misamplification factor (Sect. 2.3).

Differentiating the first equation in Eq. (19) gives the opposite conversion from D_R to D,

$$D(t) = \frac{1}{\psi'} \frac{d}{dt} [\psi D_{R}(t)] = D_{R} + D_{R}' \psi S^{2}, \qquad (20)$$

which shows that D is less (greater) than D_R wherever D_R decreases (increases) down core. R2024 recognised D_R as a "time-weighted diffusivity" and took care when interpreting their $D_R(t)$ profile; but without the analytical result in Eq. (20), inferring D from D_R is challenging. The present analysis also reveals the weighting to be highly nonlinear. In Sect. 3, we use Eq. (20) to estimate D(t) from $D_R(t)$ and Eq. (19) to predict $D_R(t)$ from D(t), discovering a marked difference between these curves.

2.3 Theory: gradient-based inversion

270

280

285

We turn to F2024's inversion for the effective diffusivity $D_{\rm F2}$, which calculates the "mean absolute gradient" \bar{m} of signals with the Barnes et al. (2003) method, which in turn is based on the diffusion-length theory of Johnsen (1977). We extend this framework to derive an exact inversion for D from \bar{m} , exposing the averaging approximation behind $D_{\rm F2}$. We find that the Barnes et al. method – and thus the $D_{\rm F2}$ estimates – require two corrections.

In the Barnes et al. (2003) method, the concentration record C is first destrained and processed to suppress unwanted signals from background climate variations. Signal peaks on the processed record, C_p , are thought to reflect the sulphate input from volcanic events more reliably (with less bias) than C. To quantify the signal variability on C_p , they studied different 10-m long sections down core by calculating their signal mean absolute gradient,

$$\bar{m} = \frac{1}{n\Delta\zeta} \sum_{i=1}^{n} \left| C_{p,i+1} - C_{p,i} \right|,\tag{21}$$

where $C_{p,i}$ denotes individual processed concentration measurements, $\Delta \zeta$ is the destrained interval between measurements, and n is the number of intervals in each 10 m. Eq. (21) is the same as their Eq. (1), despite written with different symbols.

Their method quantifies the rate of diffusive smoothing by using the observed decrease in \overline{m} down core (Fig. 1b) and retrieves D_{eff} from the rate. Notably, they regard the principal signals on C_p as periodic, with a wavenumber k^* that does not vary with depth on the destrained record (we use * to signify destraining). Accordingly, the ratio of \overline{m} of a core section at depth to the mean absolute gradient \overline{m}_0 of a reference section higher in the column measures the amplitude decay of the signals, and they equate this ratio to the signal attenuation predicted for Eq. (1) by Johnsen (1977) – thus,

295
$$\frac{\overline{m}}{\overline{m}_0} = \exp(-k^{*2}\sigma^{*2}/2)$$
, (22)

in which σ^* is the destrained value of the diffusion length σ ; that is, $\sigma^* = \sigma/S(t)$.

In Johnsen's theory, the diffusion length σ evolves according to the ordinary differential equation

$$\frac{d\sigma^2}{dt} = 2D(t) + 2\dot{\varepsilon}_z(t)\sigma^2, \tag{23}$$

and transforming this to the destrained coordinate system yields

310

$$300 d\sigma^{*2}/dt = 2D(t)/S^{2}(t). (24)$$

However, Barnes et al. (2003) took $d\sigma^{*2}/dt = 2D$ without the final $1/S^2$, assuming Eq. (23) with $\dot{\varepsilon}_z$ set to zero to be a valid diffusion-length equation for unthinned records. On taking a constant (effective) diffusivity, they then found $\sigma^{*2} = 2D_{\text{eff}}t$, which, together with Eq. (22), led them to the inversion formula

$$D_{\text{eff}} = -\frac{1}{k^{*2}t} \ln \left(\frac{\overline{m}}{\overline{m}_0} \right). \tag{25}$$

305 When rewritten for a pair of subsurface data points, this gives the F2024 inversion formula:

$$D_{\rm F2} = -\frac{1}{k^{*2}(t_2 - t_1)} \ln \left(\frac{\bar{m}_2}{\bar{m}_1} \right). \tag{26}$$

These formulas are approximate because of the missing $1/S^2$ in the underlying diffusion-length model: strictly, Eq. (24) should be used instead. In particular, for the EDC core site, the approximation is reasonable for signals in $t \leq 10^4$ yr (because $S \approx 1$ up to that age; Fig. 3a, b) but not beyond. It follows that the $D_{\rm eff}$ estimate of Barnes et al. (2003) for the Holocene ice (Fig. 1c) is approximately valid, but the $D_{\rm F2}$ estimates of F2024 for older sections of ice suffer large inaccuracies.

Having explained the Barnes et al. method, we modify it to derive an exact inversion for D. In the ψ – ζ coordinate system, Johnsen's diffusion-length equation (Eq. (23) or (24)) takes the form¹

$$\frac{d\sigma^{*2}}{d\psi} = 2D(\psi) , \qquad (27)$$

and substituting for σ^{*2} from Eq. (22) gives

315
$$D(\psi) = -\frac{1}{k^{*2}} \frac{d(\ln \overline{m})}{d\psi}$$
. (28)

This inversion formula involves a rate of change, as in the peak-based inversions, and shows that D can be estimated from the slope of the logarithmic plot of \overline{m} versus dilated age ψ (we will explore this with EDC data in Sect. 3.3).

One can again relate the effective diffusivity to D. Suppose that D in Eq. (27) equals a constant effective diffusivity, D_E ; this is the effective diffusivity that is found by the inversion without the approximation of Barnes et al. (2003) described above.

Tthen $\sigma^{*2} = 2D_E\psi$. Using this together with Eq. (22) for paired data leads to the inversion formula

$$D_{\rm E} = -\frac{1}{k^{*2}(\psi_2 - \psi_1)} \ln \left(\frac{\overline{m}_2}{\overline{m}_1} \right) \qquad \left(\equiv \frac{1}{\psi_2 - \psi_1} \int_{\psi_1}^{\psi_2} D(\psi) \ d\psi \right). \tag{29}$$

We see that D_E is the average of D over the dilated age ψ , as for D_R and D_{F1} . On comparing D_E against the effective diffusivities in Eqs. (25) and (26), we find

$$D_{\rm F2} = \frac{\psi_2 - \psi_1}{t_2 - t_1} D_{\rm E} \,, \tag{30}$$

which means that $D_{\rm F2}$ of F2024 (also $D_{\rm eff}$ of Barnes et al. 2003) is misamplified by $(\psi_2 - \psi_1)/(t_2 - t_1)$ and strongly overestimates the effective diffusivity in deep intervals (see triangle in Fig. 3c). The issue stems from the missing $1/S^2$. The misamplification ratio allows the effective diffusivities of Barnes et al. (2003) and F2024 to be corrected to give the desired value, $D_{\rm E}$.

The other correction in the mean absolute gradient approach concerns the signal wavenumber k^* . Barnes et al. (2003) and F2024 estimated it via $k^* = 2\pi/\overline{w}$, where the mean destrained wavelength \overline{w} of the signals is found by calculating

¹ Eq. (27) can also be derived from the τ – ζ formulation (Sect. 2.2.1). It is well known that given the Gaussian solution of Eq. (5), its general solution can be written as the convolution integral $f(\zeta, \tau) = \frac{1}{\sigma^* \sqrt{2\pi}} \int_{-\infty}^{\infty} F(\eta) e^{-(\zeta-\eta)^2/2\sigma^{*2}} d\eta$, where F is the initial condition (e.g. Johnsen, 1977). Substituting this into Eq. (5) yields $d\sigma^{*2}/d\tau = 2$, which, after a change of variable from τ to ψ , gives Eq. (27).

for a long record (F2024 used the Holocene or LGM part of the EDC record for this); L is the length of the record and \bar{C}_p its mean impurity concentration. Barnes et al. (2003) idealised the signals as triangular-shaped when deriving Eq. (31), but our repeat derivation in Appendix B shows that its right-hand side should be doubled, or $\pi/2$ times larger if one assumes sinusoidal signals. Consequently, their method overestimates k^* by $\approx 1.6-2$ times, and the $D_{\rm F2}$ estimates of F2024 and the $D_{\rm eff}$ estimate of Barnes et al. (2003) for Holocene ice (3.9 \pm 0.8 \times 10⁻⁸ m² yr⁻¹) are too small by a factor of $k^{*2} \approx 2.5-4$ times. In our $D_{\rm F2}$ inversions below, we remedy both issues by correcting the results with this factor and the misamplification ratio.

3 Diffusivity inversions: results and analysis

335

340

345

350

355

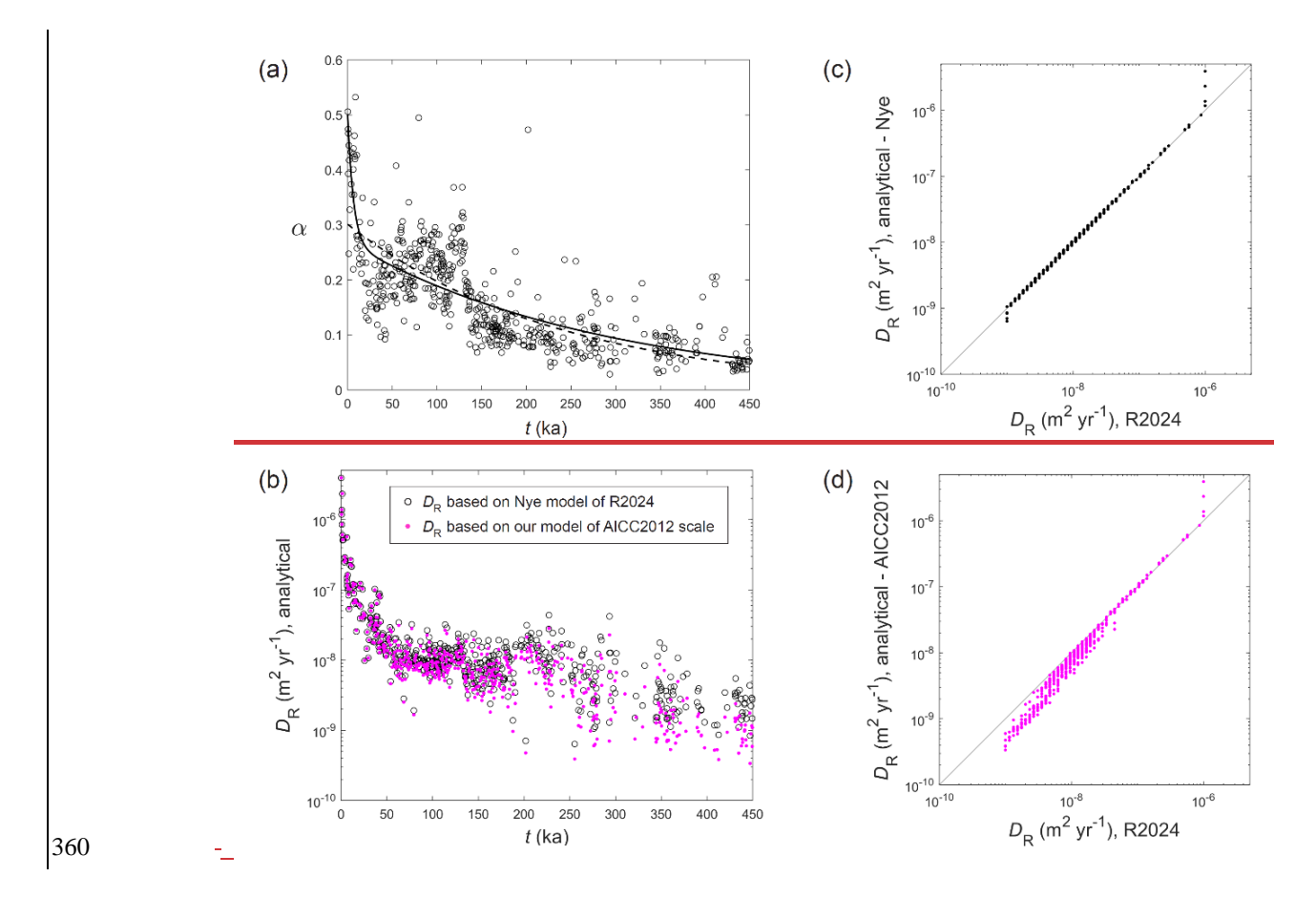
We proceed to estimate the true diffusivity profile D(t) at the EDC site, using the theory of Sect. 2 and data from F2024 and R2024 as input. The work is done in stages. In Sects. 3.1, 3.2, and 3.3, we undertake inversions from peak amplitude, peak width, and signal gradient in turn, exploring avenues including the conversion of D_{eff} to D and direct inversion of data, as well as finding the effective diffusivities D_R , D_{F1} and D_{F2} with analytical formulas. While these sections allow gleaning information about D(t), we further constrain its form by forward modelling in Sect. 3.4. In Sect. 3.5, after inferring high sulphate diffusivity confined to the firn layer, we examine how firn densification impacts the diffusivity inversion.

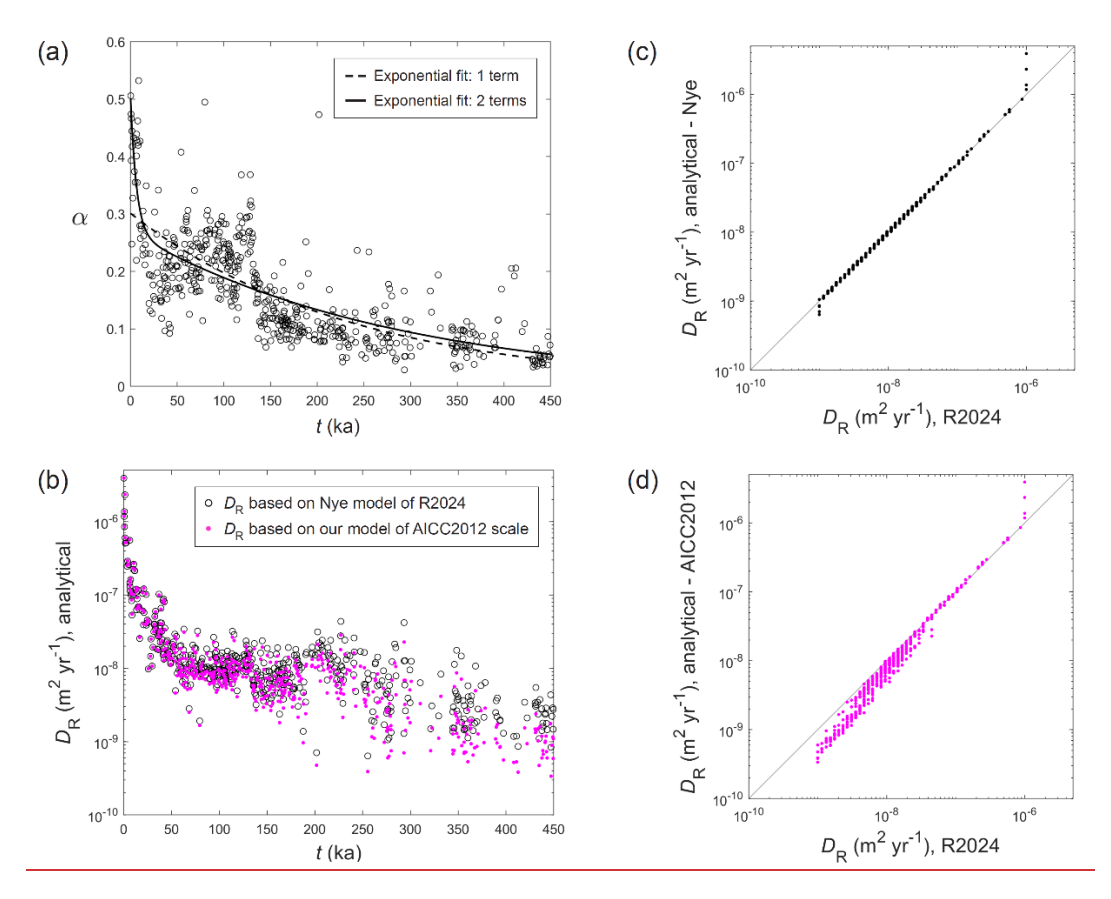
F2024 and R2024 used the AICC2012 chronology of the EDC site (Fig. 3a; Bazin et al., 2013; Veres et al., 2013) throughout data compilation and analyses. To maximise compatibility of our results with theirs, we employ the same chronology, rather than the newer AICC2023 chronology (Bouchet et al., 2023). In particular, our inversions use what we call "AICC2012-based" functions – smoothed forms of the thinning factor S and dilated age $\psi(t)$ (Fig. 3, magenta curves), which we derive from a power-law model of the ice submergence velocity in the EDC column fitted to the AICC2012 age–depth scale; see the caption of Figure 3 for the details. Although the smoothing injects minor differences between our $D_{\rm eff}$ estimates and those of R2024 and F2024, it is desirable because the thinning function provided with the AICC2012 dataset is non-monotonic (black curve, Fig. 3b), with small bumps that imply negative strain rate at various depths.

3.1 Inversions from peak-amplitude decay

Figure 4a shows the relative amplitudes α of the peaks studied by R2024, obtained from their Supplementary data by dividing observed peak heights by original peak heights. The values show considerable scatter but generally decay with age.

To compute the effective diffusivity D_R for each peak, we apply Eq. (15) to its α -value, setting τ_0 as described in Sect. 2.2.1. When calculating the strain rate $\dot{\varepsilon}_z$ for simulating Eq. (1), R2024 adopted an ice submergence velocity profile derived not from the AICC2012 scale, instead from a Nye model with an ice thickness of 3165 m and a surface accumulation rate that puts the peak at its observed depth, so that its age and depth agree with the AICC2012 scale. Thus, their inversion of D_R envisages a slightly different steady-state ice column for each peak. Their use of the Nye model, which does not resolve the





370

375

Figure 4. Analytical inversion for the effective diffusivity D_R from the peak-amplitude data of Rhodes et al. (2024). (a) Amplitude ratio α versus age t for 537 peaks. Dashed curve plots best-fit exponential $\alpha(t) = 0.301 \exp(-4.22 \times 10^{-3}t)$; solid curve, best-fit exponential sum $\alpha(t) = 0.232 \exp(-0.157t) + 0.268 \exp(-3.49 \times 10^{-3}t)$. (b) Computed D_R values versus age. Black circles plot results of the inversion assuming the Nye model of Rhodes et al. (2024); magenta points plot results of the inversion assuming our AICC2012-based ice-flow functions in Fig. 3. Following Rhodes et al. (2024), each D_R value is plotted at the age of the observed peak, rather than as a bar spanning the period over which it applies. (c) Scatterplot of the black-circled D_R values in (b) against the D_R estimates of Rhodes et al. (2024), which they found by simulating Eq. (1) to match peak-amplitude decay. (d) Scatterplot of the magenta D_R values in (b) against the D_R estimates of Rhodes et al. (2024).

details of firn compaction near the top of the column, seems consistent with their choice of working with ice-equivalent depths when compiling original peak amplitudes (Sect. 2.2.1). We shall say more about the effect of the firn processes in Sect. 3.5.

To show that our analytic approach can reproduce the D_R estimates of R2024, in our first use of Eq. (15) we adopt their ice-flow approximation by using $\psi(t)$ based on their peak-specific Nye model instead of our AICC2012-based model. The corresponding D_R results (Fig. 4b, circles) agree closely with their estimates (Fig. 1c), decaying from $\sim 10^{-6}$ to $\sim 10^{-9}$ m² yr⁻¹,

rapidly in ≈ 0 –50 ka and slowly beyond. We find four values exceeding 10^{-6} m² yr⁻¹ near t = 0 and four values below 10^{-9} m² yr⁻¹ not reported by R2024 (Figs. 4c and 4b). These and other minor discrepancies between our results arise because Eq. (15) is an exact formula for D_R , whereas their D_R estimates are constrained to 50 graded values (visible from the banding in Fig. 4c) on the log scale between 10^{-9} and 10^{-6} m² yr⁻¹ (values outside these bounds are clipped to them).

Performing the same inversion with our AICC2012-based function $\psi(t)$ (Fig. 3c) yields lower D_R estimates, especially for deeper peaks (Fig. 4b & d, magenta points). This is because their Nye model tends to overestimate S (underestimate the amount of thinning) at depth; less of the thinning-induced enhancement in signal diffusion (Sect. 2.2.2) is captured, making their D_R estimates larger. The lowering helps explains some of the difference between D_R and F2024's D_{eff} estimates.

380

385

390

395

400

405

Next, we attempt to estimate the true diffusivity profile D(t) by two approaches. The first applies the time-domain inversion in Eq. (7) (same as Eq. (11) in the ψ – ζ domain) to a smoothed version of α , which we derive by fitting the α -data with the sum of two exponentials (solid curve, Fig. 4a). This function is preferred to a single exponential (dashed curve, Fig. 4a) because it captures the high α -values near t = 0 better. In Eq. (7) we use the AICC2012-based thinning function S (Fig. 3b).

The second approach converts D_R to D with Eq. (20), assuming the AICC2012-based function ψS^2 (Fig. 3d). To derive a smooth input for Eq. (20), in which the derivative D_R' appears, we spline-fit our AICC2012-based D_R estimates from Fig. 4b on log-10 scale. These estimates show pronounced fluctuations and scatter on time scales shorter than ≈ 20 kyr that indicate uncertainty and noise on the relative amplitudes α , so we choose a level of spline smoothing to suppress these fluctuations; see Spline 2 in Fig. 5b, e, h. However, the exact time scales on which fluctuations in D_R reflect true changes in diffusivity is unknown, so we experiment also with less and more smoothing by using Spline 1 and Spline 3 (the left-hand and right-hand columns of panels in Fig. 5). Spline 3 strongly suppresses fluctuations in D_R shorter than about 50 kyr.

The curves of D(t) computed by this second approach (Fig. 5, solid black curves) indicate high, steeply-decaying diffusivity in the first ≈ 2 to 8 ka – from $\sim 10^{-6}$ m² yr⁻¹ to well below 10^{-7} m² yr⁻¹, followed by generally low diffusivity beyond ($\sim 10^{-8}$ m² yr⁻¹) and even negative diffusivity in some age ranges (see comments below). Although stronger spline smoothing lengthens the initial fast decay, all three curves portray D as greatly diminished from its surface value by several ka (Fig. 5d–5i). Because the firn-ice transition at EDC lies at ≈ 100 m depth (e.g. Landais et al., 2006; Calonne et al., 2022), where $t\approx 2.5$ ka, much of the initial steep drop in D apparently occurs in the firn layer; we explore the cause of this later in Sect. 4.1. In contrast, D(t) retrieved by from the first approach (Fig. 5, dashed black curve in all panels, Fig. 5) shows a much more subdued decay over the first 30 ka, starting from a lower surface diffusivity $\approx 6 \times 10^{-8}$ m² yr⁻¹. We think that this is because the dual two-term exponential function-in Fig. 4a does not adequately capture the high negative slope of the α -data near t=0, which is necessary for Eq. (7) to reconstruct the details of D there.

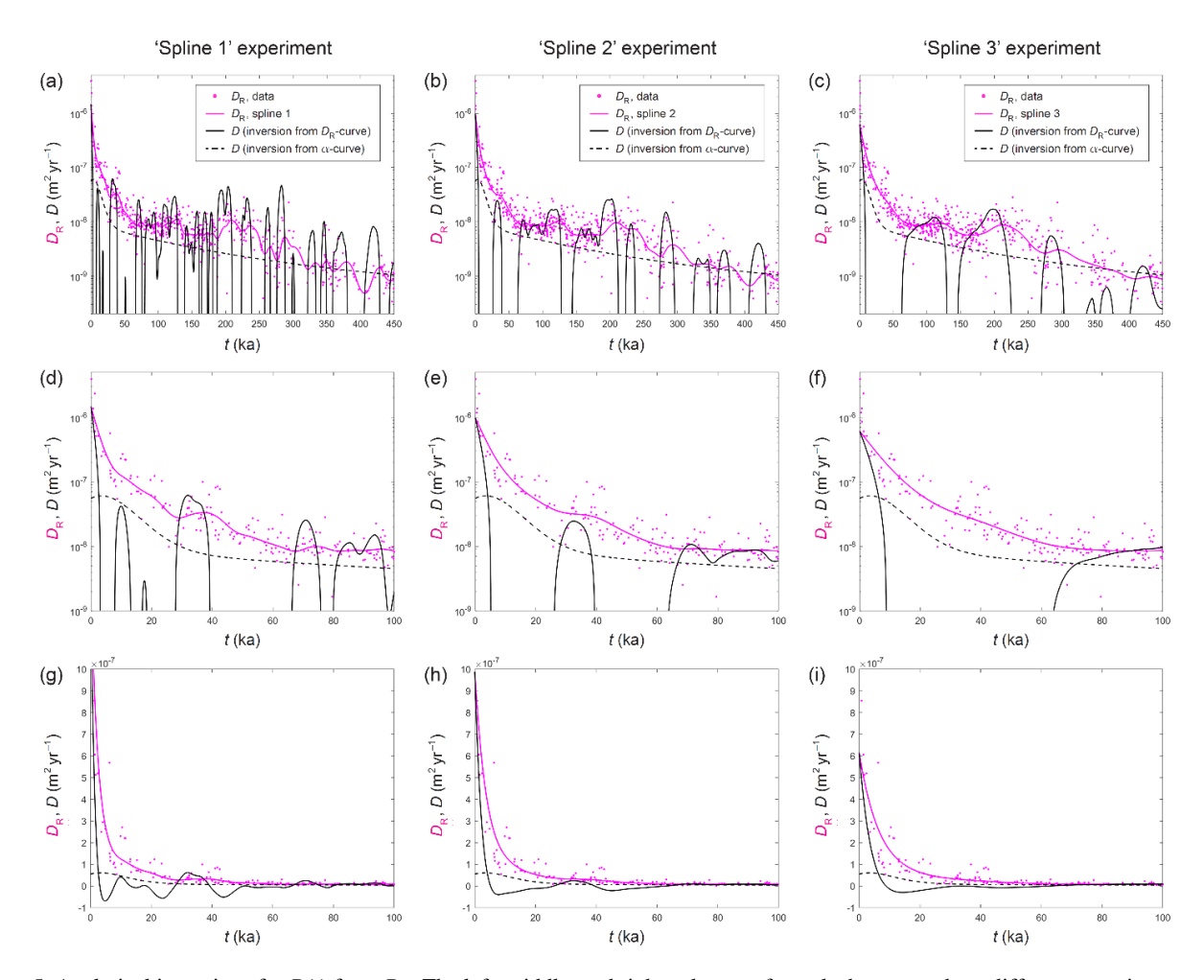


Figure 5. Analytical inversions for D(t) from D_R . The left, middle, and right columns of panels document three different experiments where the curves of D_R serving as input to the inversion ("Splines 1, 2 and 3"; magenta curves) have been derived by spline-fitting the D_R point data at different smoothness. The level of spline smoothing increases from left to right. In each panel, magenta circles plot the D_R data from Fig. 4b; black curve shows D(t) obtained by using Eq. (20) with the chosen spline for D_R ; dashed black curve shows D(t) obtained by using Eq. (7) with the two-termeompound exponential curve of α in Fig. 4a as input. Each row of panels displays results on the same axes: (a–c) over 450 ka; (d–f) over the last 100 ka in log scale; (g–i) over the last 100 ka in linear scale.

In the second approach, the curves of D(t) lie below the D_R estimates in many places. As expected from our theory in Sect. 2.2.2, D(t) lies above (below) the spline curve of D_R where this curve rises (drops). Where D_R increases with age, high $D(t) > D_R$ is retrieved because peaks with much lower amplitude than overlying peaks in the column imply high diffusivity in the intervening depth interval. Where D_R decreases with age, low $D(t) > D_R$ is retrieved because peaks with undiminished (or higher) amplitudes compared to overlying peaks can be explained only by low (or negative) diffusivity in the intervening interval. In this connection, a robust feature of all three curves of D(t) is that they and their initial steep drops lie well below

the curves of D_R in the first few tens of ka, where the D_R estimates decay much more gradually (Fig. 5d–5i). This feature, which remains if we use the D_R values of R2024 as input to the conversion, implies that D_R contains a long memory of the initial high diffusivities. We anticipated this memory effect in Sect. 2.2.2. Here, it operates because the effective diffusivity D_R "remembers" the initial rapid lowering of the peaks by fast diffusion during their first few thousand years of evolution, which cannot be undone however slow is diffusion afterwards. This finding is supported by the relative amplitudes in Fig. 4a, which evidence more than 40 % reduction in peak height (α < 0.6) on even the shallowest peaks.

The second inversion approach is not without limitations. First, the real original sulphate peaks at the surface might have durations (FWTMs) different from the 3 years assumed in the inversion and durations different from each other, as shown by the large scatter in the α and D_R values. Second, the level of spline smoothing is uncertain. Indeed, it may not be possible to obtain the ideal input – one giving the true D(t) profile – by smoothing the D_R estimates at all age by an equal amount. Of the three inversion experiments, we regard the one with Spline 2 as giving more reliable insights about D(t), because Spline 1 yields many short fluctuations on D(t) that are likely spurious (Fig. 5a), and Spline 3 strongly underrepresents the decrease of the D_R estimates near t = 0 (Fig. 5f & 5i). Third, the inversion does not constrains D(t) poorly well after its initial drop; there, D going negative and oscillating about zero is unphysical, although the experiments generally indicate D as very low, the stretches of negative D, which generally reflect low D ($< D_R$), are unphysical. Occurring where the D_R curves—Some ofdrop rapidly with age, th-the stretches of negative D stretchesmay arise from estimation noise/errors on the input D_R values, incorrect splining of-those values, and may be due to a non-steady column, whose in which strain-rate profile varied with time or where different ice layers of ice inherited properties (e.g., grain size, dustiness) that led them to have different diffusivity histories. Our steady-state model does not account for sSuch-inheritance—variations-cannot be reconstructed from the stretches with our steady-state model and might therefore yield negative D in an inversion.

In summary, estimating D from D_R has been possible due to the memory effect. Fast diffusion in the shallow subsurface reaching back a few ka (in the firn?) seems responsible for the elevated values of D_R for $t \lesssim 50$ ka reported by R2024. Consequently, sulphate diffuses rapidly only near the top ≈ 100 m, not across the whole of the Holocene stretch of the EDC column. In Sect. 3.4, we will back out D(t) by going the other way – forward modelling from D to D_R , which reveals how the memory preconditions a long tail on D_R at EDC, whose continuation to several hundred ka is perceptible in Figs. 1c and 4b.

3.2 Inversions from peak widening

430

435

445

To calculate $D_{\rm Fl}$ analytically, we use Eq. (16) with input data for τ and ψ from paired depths (Sect. 2.2.2); for these, we use the τ values of sulphate peaks derived from the destrained FWHMs measurements of F2024 (Fig. 6a) and the AICC2012-based function $\psi(t)$. As noted in Sect. 1, F2024 treated interglacials and glacial maxima separately and used the median FWHM of the peaks in each period as the input to their inversions. Here we explore a variation to their scheme, by calculating the $D_{\rm Fl}$

values for all paired combinations of individual peaks from each two periods being studied, which allows us to find the median $D_{\rm F1}$ and the associated uncertainty (interquartile range in $D_{\rm F1}$) for each interval.

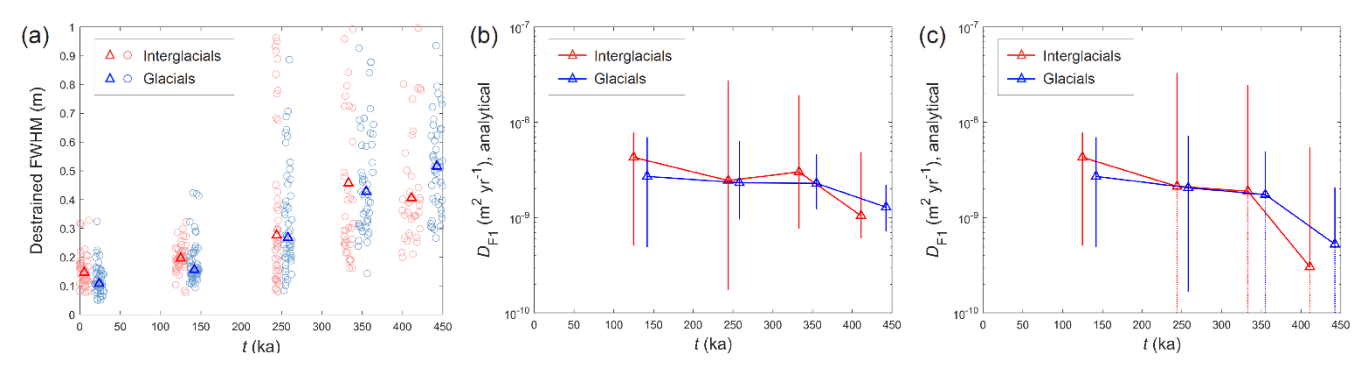


Figure 6. Analytical inversion of effective diffusivity D_{F1} from peak widths in interglacial and glacial maximum periods. (a) Destrained full width at half maximum (FWHM) of individual peaks, plotted against age (circles); data from Fudge et al. (2024). Triangle plots the median FWHM of each period. (b & c) D_{F1} computed from the data in (a) with Eq. (16). Triangles plot median values; and vertical bars, interquartile ranges (dotted if the lower quartile is negative and cannot be shown on logarithmic scale). The inversions in (b) study intervals between the Holocene and earlier interglacials (red) and between the LGM and earlier glacial maxima (blue). The inversions in (c) study intervals between successive interglacials or successive glacial maxima. Each triangle is plotted at the age of the older of each two periods.

455

465

470

In a first set of inversions, we follow F2024 by referencing each older interglacial or glacial maximum period to the most recent period, so every interval studied includes the Holocene or LGM part of the core. These inversions yield median D_{F1} values ≈ 1.0 – 4.3×10^{-9} m² yr⁻¹ (Fig. 6b), agreeing overall with F2024's results (1.6– 6.0×10^{-9} m² yr⁻¹; their Table 1), although our glacial-maxima values (1.3– 2.7×10^{-9} m² yr⁻¹) are lower than theirs (4.0– 5.5×10^{-9} m² yr⁻¹). Our scheme variation and the smoothing behind $\psi(t)$ explain the minor differences between our results and F2024's results.

In a second set of inversions, we reference each period to the next younger period, to study how D_{F1} varies with depth. Interestingly, these inversions (Fig. 6c) yield median D_{F1} values that decrease more clearly with age – to less than 10^{-9} m² yr⁻¹ beyond 400 ka, although the uncertainties are large. The trend may indicate a real decline in the true diffusivity down core because these D_{F1} results pertain to successively deeper intervals (the shallowest results at 125 ka and 142 ka are necessarily unchanged from those in Fig. 6b). In contrast, D_{F1} in the first set of inversions always includes a memory of the high diffusivities of the shallowest results; recall that the effective diffusivities are interval averages of D (Sect. 2.2.2). Thus, the use of Holocene/LGM as the reference period explains why D_{F1} in Fig. 6b and the D_{F1} results of F2024 are roughly level, at most hinting at a decline.

3.3 Inversions from mean absolute gradient, \bar{m}

475

480

485

490

495

To find D_{F2} and D_{E} analytically, we use Eqs. (26) and (29), with the data from F2024 for \overline{m} in different ice sections in interglacials and glacial maxima (Fig. 7a) and the signal wavenumbers k^* measured by them for these periods, 33.3 m⁻¹ and 32.7 m⁻¹, respectively. As with D_{F1} , we calculate D_{F2} and D_{E} for all paired combinations of input data from each two periods,

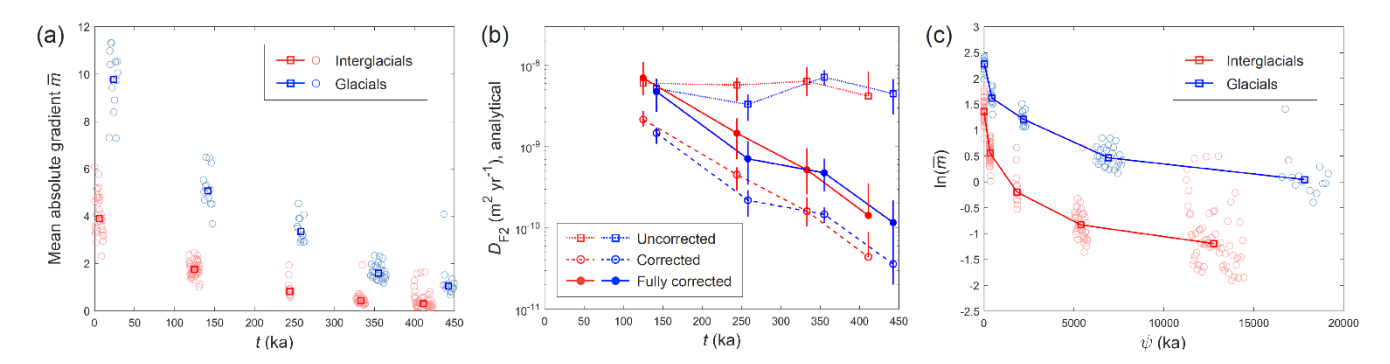


Figure 7. Inversion of effective diffusivity D_{F2} from mean absolute gradient \bar{m} of signals in interglacial and glacial maximum periods. (a) \bar{m} of multiple ice stretches in each period, plotted against age; data from Fudge et al. (2024). Square plots the median \bar{m} of each period. (b) D_{F2} values computed from the mean absolute gradient data with Eq. (26) ("uncorrected"), with Eq. (29) ("corrected", i.e., D_E values), and with Eq. (29) and a further multiplication by 2.5–4 times ("fully-corrected"; the multiplicative range extends the uncertainty around each value). All of these inversions study the intervals between successive interglacials (red) and between successive glacial maxima (blue), as in Fig. 6c. Symbols plot median values, and vertical bars plot interquartile ranges; the lower quartile is missing if it is negative and cannot be shown on log scale. (c) $\ln(\bar{m})$ against the AICC2012-based dilated age ψ for the periods studied. The squares plot median values.

to gauge the uncertainty around each median. Given a key interest is how these effective diffusivities vary with depth, and both are interval averages (Sect. 2.3), we reference each period to the next younger period in these inversions.

Recall that D_{F2} is the uncorrected effective diffusivity, equivalent to F2024's estimate, and D_E corrects D_{F2} for misamplification by the factor $(\psi_2 - \psi_1)/(t_2 - t_1)$, which is larger the older is the interval (Sect. 2.3). Indeed, the inversion results in Fig. 7b show that whereas the median D_{F2} values ($\approx 3.3-7.2 \times 10^{-9} \text{ m}^2 \text{ yr}^{-1}$; squares) are broadly level and consistent with the D_{F2} estimates of F2024 (4.8–6.1 \times 10⁻⁹ m² yr⁻¹; see their Table 1), the median D_E values (open circles) decrease with age and are much lower than D_{F2} . The difference attests a strong overestimation in D_{F2} , even for the shallowest results at 125 and 142 ka. We further correct D_E for the issue with k^* in the Barnes et al. (2003) method by multiplying them by 2.5–4 (Sect. 2.3). This yields the "fully-corrected" D_{F2} estimates in Fig. 7b (filled circles). This correction returns the shallowest results roughly to the uncorrected D_{F2} medians. But the strong decreasing trend remains: the deepest fully-corrected estimates at \approx 400 ka are

nearly 2 orders of magnitude less than the shallowest values. The uncertainties in Fig. 7b are relatively small, so the trend cements the finding from D_{F1} (Sect. 3.2) that the true diffusivity decreases with age.

This decrease in D is confirmed separately by the exact inversion $D = -(1/k^{*2})d(\ln \bar{m})/d\psi$ in Eq. (28). Figure 7c plots $\ln(\bar{m})$ against dilated age ψ , showing a reduction of the slope of the plot trajectories – and thus D – with age. For both interglacials and glacial maxima, the slopes of the segments linking the plot points essentially give the fully-corrected D_{F2} estimates of Fig. 7b. Since a smooth curve through the points won't deviate much from the segments, D(t) is well approximated by these estimates (more precisely, D will be somewhat less than these estimates, as the local slope of the curve through each point would be shallower than the segment leading left from it). Consequently, the fully-corrected D_{F2} results in Fig. 7b approximately describe how the true diffusivity varies from ≈ 100 to 400 ka. These results, except perhaps the shallowest interglacial result, should be free from bias by the high, steeply decreasing D in the shallow subsurface inferred in Sect. 3.1.

The deepest values of \overline{m} that we use from F2024 (between 400 and 450 ka, Fig. 6a) might include signal variability from the anomalous trough-sided peaks at depths $\gtrsim 2700$ m (Sect. 1). If so, our deepest two fully-corrected $D_{\rm F2}$ values in Fig. 7b would be underestimated, but this does not affect the decreasing trend in 100–360 ka. Also, any underestimation is probably limited because F2024 found an unusual increase in \overline{m} only in ice older than 550 ka (their Fig. 6). Our $D_{\rm F1}$ results (Sect. 3.2) may be also corrupted by the anomalous peaks, but, as noted next, will not be used in our final inversion.

3.4 Forward modelling to estimate D(t)

500

505

510

515

520

525

So far, we learned that the true diffusivity D drops steeply in the first few ka from $\approx 10^{-6}$ m² yr⁻¹ by at least an order of magnitude (Fig. 5h; Sect. 3.1) and decays further from ≈ 100 –450 ka, roughly following the fully-corrected median $D_{\rm F2}$ estimates (Fig. 7b; Sect. 3.3). What profile of D(t) with these characteristics best explains the effective diffusivity estimates $D_{\rm R}$ and $D_{\rm F2}$ (after full correction)? Can it explain these simultaneously, and thus reconcile R2024's and F2024's findings?

To study this, we use Eq. (19) to predict the $D_R(t)$ profile from D(t), posing the following form for D(t) on the semi-logarithmic plot. Starting from 10^{-6} m² yr⁻¹ at t = 0, it decreases linearly to a corner value D_c , at age t_c , followed by either a flat floor ($D = D_c$) or an inclined floor for $t > t_c$. The inclined floor is assumed to have a slope equal to the mean slope of the fully-corrected median D_{F2} estimates (Fig. 7b), but its level is fixed by the corner location, not by the estimates. For either floor type, we find the combination of D_c and t_c that best-fits the $D_R(t)$ profile to our AICC2012-based D_R estimates (Fig. 4b, magenta points). The D_{F1} results (Fig. 6c) are excluded from the exercise, given their large uncertainties.

Figure 8 shows the best-fit profiles and maps of misfit over the t_c – D_c parameter space from the forward modelling. In the flat-floor experiment (Fig. 8a, c), the predicted $D_R(t)$ profile fits the D_R estimates moderately well, and D decreases from its surface value to the corner diffusivity $D_c \approx 2.1 \times 10^{-9} \text{ m}^2 \text{ yr}^{-1}$ in 9.1 ka. In the inclined-floor experiment (Fig. 8b, d), $D_R(t)$ fits the D_R estimates better, capturing their gentle decay trend at large t. Here, D(t) has a shorter initial drop (2.8 ka), D_c is higher ($\approx 1.74 \times 10^{-8} \text{ m}^2 \text{ yr}^{-1}$), and the floor shoots through the fully-corrected D_{F2} values even though their level is not a fitting

target; D(t) also lies slightly below their trend, as anticipated. Thus, this D(t) profile (Fig. 8b) explains the mean absolute gradient data as well as the peak-amplitude data and yields the better reconstruction of the two experiments. It also gives a more plausible estimate of the true diffusivity than the opposite conversion from D_R to D (Sect. 3.1), which reconstructed negative D intervals. Its steep initial drop is mainly constrained by the D_R decay in 0–50 ka, and its inclined-floor level by the

530

535

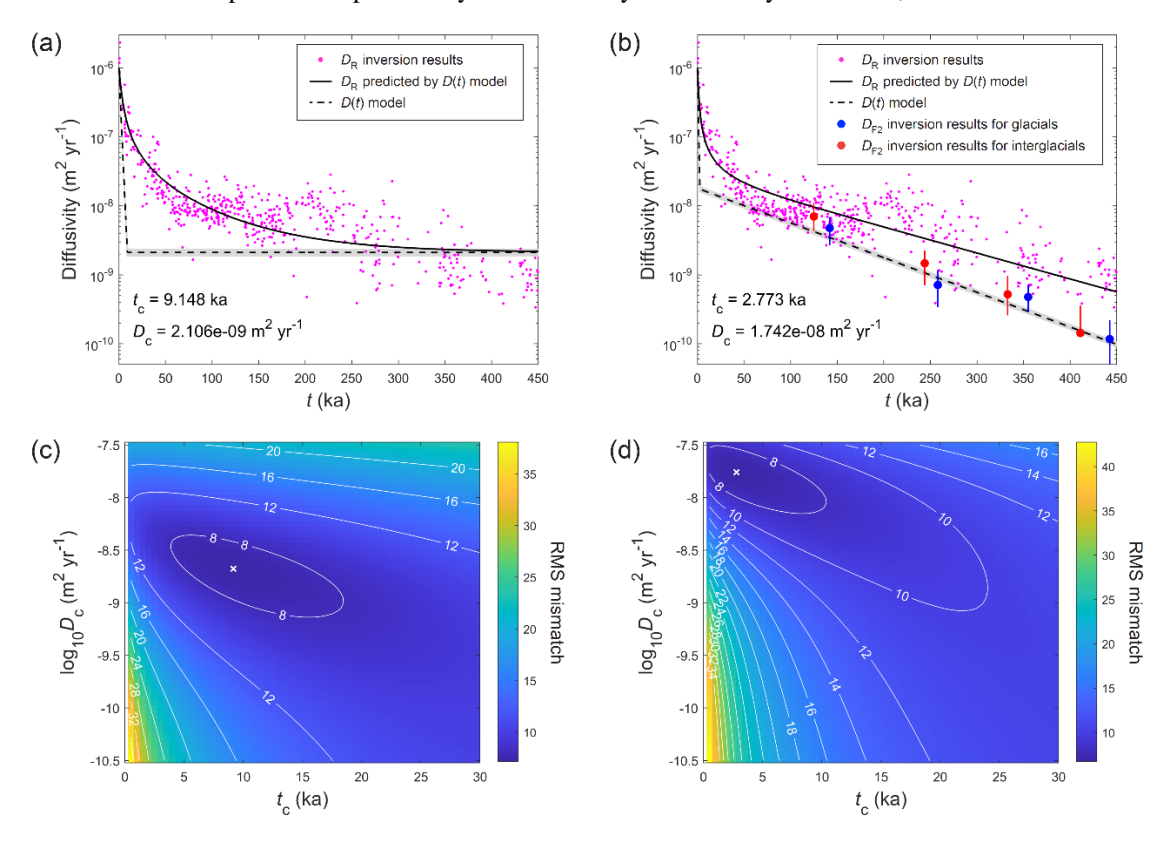


Figure 8. Forward modelling of the effective diffusivity profile $D_R(t)$ from the true diffusivity profile D(t), and least-squares fitting to constrain D(t). As described in Sect. 3.4, panels (a) and (c) report an experiment assuming a flat floor for D; and panels (b) and (d), an inclined floor. (a, b) Plot of log diffusivity versus age, showing D(t) (dashed), the predicted $D_R(t)$ profile (solid curve), and D_R data from peak-amplitude inversion (points). Panel (b) includes the fully-corrected D_{F2} results of Fig. 7b for comparison. Grey shading about D(t) shows its maximal variation as found from the confidence intervals of the best-fit parameters, t_C and t_C (c, d) Root mean square (RMS) mismatch in log-10 scale between predicted and estimated t_C values, as a function of the corner age t_C and corner diffusivity t_C of the t_C profile. White crosses locate the optimal t_C and t_C values in (a) and (b), which yield RMS mismatches of 7.16 and 6.70, respectively.

deeper D_R values. Importantly, the corner age (2.8 ka) confirms our finding from Sect. 3.1 that the high D decaying through the upper column does not extend far below the firn-ice transition. Note that D(t) in Fig. 8b is reliable to a maximum age of only ≈ 390 ka (≈ 2700 m) because the deepest D_R and fully-corrected D_{F2} data constraining the fit are interval-based results.

In these experiments, the long tails on D_R caused by the high initial D values confirm the memory effect, and the D(t) profiles are broadly consistent with the Holocene D_{eff} estimate of Barnes et al. (2003), $\approx 1.3 \pm 0.6 \times 10^{-7} \,\text{m}^2\,\text{yr}^{-1}$ after applying the k^* -correction (Sect. 2.3). That D(t) in Fig. 8b lies below the D_R , D_{F1} and D_{F2} estimates of R2024 and F2024 by up to 1–2 orders of magnitude confirms that these effective diffusivities approximate D crudely, and that the discrepancy between them stems from the underlying averaging, the different intervals used to evaluate them, and errors in the mean absolute gradient method.

Finally, the D_R estimates being fitted depend on the assumed 3-year FWTM duration for the surface peaks (Sect. 2.1). To gauge the impact of this assumption, we conducted an ensemble of 10^5 best-fit forward model runs, where each of the 537 D_R estimates serving as fitting target in each run was picked randomly from its three values based on FWTMs of 1, 3, and 5 years. The maximal ranges found for t_c and D_c are 2.3–2.9 ka and 1.70–1.78 \times 10^{-8} m² yr⁻¹, respectively, narrowly bracketing the results in Fig. 8b. This is not surprising as D_R is weakly sensitive to the FWTM, as found by R2024.

3.5 Diffusivity inversion in the firm

545

550

565

570

The preceding inversions highlight the firn diffusivity as a key interest, but their methods ignore firn densification and assume an EDC column consisting of ice only. Might the high D found for the firn be an artefact of this neglect? Should the methods be adjusted to account for firn density change? The D_R inversion is especially relevant in this regard, as it involves signals descending through the firn layer; its results are also used in the estimation of D(t) (Sect. 3.1 and 3.4). Here we show that because of the way the bulk concentration C is defined and used, Eq. (1) correctly describes signal evolution in the firn as well as in the ice, so that the D_R inversion and our findings for D are valid.

The concerns are two-fold. R2024's reconstruction of the original surface peaks, which provides input data for the D_R inversion and takes each peak's width (FWTM) to be 3a, uses the ice-equivalent thickness and assumes surface material with the ice density ρ_i (917 kg m⁻³) throughout calculation (Sect. 2.2.1). If the firn surface density ρ_0 (< ρ_i) is used in the reconstruction, each original peak would be wider ($3a\rho_i/\rho_0$), its height proportionally less, so α may have been underestimated and D_R overestimated. A second concern is that Eq. (1) might not conserve the amount of impurity in densifying firn. With D defined as the diffusivity of the bulk material (ice–air composite in the case of firn), $D\partial^2 C/\partial z^2$ in Eq. (1) describes impurity flux divergence only if C is the impurity amount *per unit volume* of bulk material, not if C is impurity amount *per unit mass* – as used by us and R2024 in the D_R inversions. Consequently, one fears that Eq. (1) might be the wrong model, and it is unclear whether D presently retrieved for the firn describes its bulk diffusivity or some other quantity.

We dispel these concerns in the following by deriving Eq. (1) from first principles. Consider the firn layer in the Cartesian coordinates (X, Y, Z), with depth Z measuring down from the surface. Let $\mathbf{U} = (U, V, W)$ be the firn velocity, and $\rho = \rho(Z)$ be

the firn density profile, assumed time-invariant. We define the bulk concentration c_B as the impurity amount per *volume*, i.e., $c_B = \rho C$. Then, impurity conservation obeys

$$\frac{\partial c_{\rm B}}{\partial t} + \nabla \cdot (\mathbf{U}c_{\rm B}) = \nabla \cdot (D\nabla c_{\rm B}), \tag{32}$$

575 in which D = D(Z) describes the vertical diffusivity profile, and the equation for water mass conservation is

$$\frac{\partial \rho}{\partial t} + \nabla \cdot (\rho \mathbf{U}) = 0 . \tag{33}$$

At ice-sheet divide or summit locations, ρ , c_B and W have negligible horizontal variations (they are functions of Z only) so the above equations become

$$\frac{\partial \rho}{\partial t} + W \frac{\partial \rho}{\partial \mathbf{Z}} + \rho \nabla \cdot \mathbf{U} = 0 , \qquad (34)$$

$$580 \quad \frac{\partial c_{\rm B}}{\partial t} + W \frac{\partial c_{\rm B}}{\partial Z} + c_{\rm B} \nabla \cdot \mathbf{U} = \frac{\partial}{\partial Z} \left(D \frac{\partial c_{\rm B}}{\partial Z} \right) , \tag{35}$$

where W = W(Z) is the submergence velocity profile in the column.

Now suppose the depth–age scale Z = g(t), with the function g given by

$$t = g^{-1}(Z) = \int_0^Z \frac{d\eta}{W(\eta)}.$$
 (36)

We define z = Z - g(t) in order to use the reference frame of Eq. (1), which follows the material as it descends. The variable change from Z to z gives $\partial/\partial Z \rightarrow \partial/\partial z$ and $\partial/\partial t \rightarrow \partial/\partial t - W(g(t))\partial/\partial z$, and Eqs. (34) and (35) become

$$\frac{\partial \rho}{\partial t} + \tilde{w} \frac{\partial \rho}{\partial z} + \rho \left(\frac{\partial U}{\partial X} + \frac{\partial V}{\partial Y} + \frac{\partial W}{\partial z} \right) = 0 , \qquad (37)$$

$$\frac{\partial c_{\rm B}}{\partial t} + \tilde{w} \frac{\partial c_{\rm B}}{\partial z} + c_{\rm B} \left(\frac{\partial U}{\partial X} + \frac{\partial V}{\partial Y} + \frac{\partial W}{\partial z} \right) = \frac{\partial}{\partial z} \left(D \frac{\partial c_{\rm B}}{\partial z} \right) . \tag{38}$$

In this reference frame, material seen from the horizon with age t has the velocity

$$\widetilde{w}(z,t) = W(g(t)+z) - W(g(t)). \tag{39}$$

On the short length scale of the signals ($\sim 10^{-1}$ – 10^0 m), the vertical gradient of velocity W can be approximated by the strain rate, so $\tilde{w} \approx \dot{\varepsilon}_z(t)z$. Density and diffusivity variations across individual signals can be assumed to be small on this scale, so we take $\partial \rho/\partial z \approx 0$ and $\partial (D\partial c_B/\partial z)/\partial z \approx D\partial^2 c_B/\partial z^2$. Applying the first of these approximations in Eq. (37) yields the compaction relation $\partial U/\partial X + \partial V/\partial Y + \partial W/\partial z = -(\partial \rho/\partial t)/\rho$, which, when used in Eq. (38), converts it to

$$\frac{\partial c_{\rm B}}{\partial t} - \frac{c_{\rm B}}{\rho} \frac{\partial \rho}{\partial t} = D \frac{\partial^2 c_{\rm B}}{\partial z^2} - \dot{\varepsilon}_z(t) z \frac{\partial c_{\rm B}}{\partial z} \,. \tag{40}$$

This is an approximate general evolution model for signals on $c_{\rm B}$ in firn or ice.

In the ice, where $\rho \equiv \rho_i$ (constant), Eq. (40) loses the compaction term and reduces to the same form as Eq. (1). This means that Eq. (1) is valid in the ice whether the bulk impurity concentration is defined in per mass or volume terms.

In the firn, Eq. (1) is missing the compaction term of Eq. (40) so it cannot be used to track c_B . But by substituting $c_B = \rho C$ into Eq. (40), we recover Eq. (1) exactly after some algebra. This means that Eq. (1) is valid in the firn and is the right model for formulating the diffusivity inversion, provided that C measures the bulk impurity concentration in per mass terms, as done by R2024 and us here. Inversions with the impurity concentration in per volume terms must use Eq. (40) instead.

It follows that R2024's reconstruction of the original peaks gives the right inputs, and the D_R inversion is valid for both peaks in the firn (which experienced diffusion in a densifying material) and peaks in the ice (which experienced diffusion in a densifying material and then diffusion under constant density). A further realisation unknown to the earlier studies is that D retrieved for the firn by inversions based on Eq. (1) automatically quantifies its bulk diffusivity. It thus turns out fortunate that R2024 used the chemical measurements expressed as sulphate concentration in per mass terms directly as C in Eq. (1).

4 Physical controls on sulphate diffusion at EDC

Armed with D(t) in Fig. 8b, we discuss the mechanisms of sulphate transport in the EDC column, going beyond the interpretations made by R2024 and F2024 from their effective diffusivities. D drops steeply from its surface value $\approx 10^{-6}$ m² yr⁻¹ to $\approx 1.7 \times 10^{-8}$ m² yr⁻¹ at 2.8 ka, an age coinciding roughly with the firn base (≈ 2.5 ka at 100 m depth); this drop is much shorter in duration than the initial decay in D_R (Figs. 1c and 4). A slower decay in D to $\sim 10^{-10}$ m² yr⁻¹ follows from 2.8–390 ka, although its real form may not be exactly log-linear as posited in our forward model; D is similar at ≈ 125 ka to the D_{F1} and D_{F2} estimates of F2024 (1.6–6.1 \times 10⁻⁹ m² yr⁻¹) but much lower in deeper ice. We consider these intervals in turn.

4.1 Vapour diffusion in the firm

600

605

620

Recall that *D* retrieved for the firn reflects its bulk diffusivity (Sect. 3.5). We interpret the high *D* on the steep drop as being due to diffusion of H₂SO₄ vapour through interconnecting air pores in the firn. This mechanism is plausible because H₂SO₄, though often viewed as nearly non-volatile, does have a vapour pressure (Tsagkogeorgas et al., 2017).

A back-of-the-envelope calculation of the diffusion rate involving the H_2SO_4 vapour pressure p_v and H_2SO_4 diffusion coefficient Ω_a in firn air supports the interpretation. We assume H_2SO_4 transport by vapour diffusion to be much faster than solid-state diffusion of sulphate through ice grains, but slow compared to sulphate exchange between ice and air, such that vapour diffusion is rate limiting. This assumption, which is justified by the time scales found below, features also in the Whillans and Grootes (1985) model for water isotope diffusion in firn, except evaporation replaces fractionation of the species

here. To estimate p_v , we assume sulphuric acid to be available on firn grain surfaces to exchange with vapour; then, Eq. (11) of Tsagkogeorgas et al. (2017) gives $p_v \sim 5 \times 10^{-9}$ Pa at -53 °C. To estimate Ω_a , we extrapolate the H₂SO₄ diffusion coefficients measured by Brus et al. (2017) at 278–298 K under laminar conditions to ≈ -50 °C, finding $\Omega_a \sim 0.015$ to 0.05 cm² s⁻¹ or ~ 45 to 150 m² yr⁻¹ when bearing in mind the uncertainty in its power-law temperature dependence noted by these authors (see their Fig. 5 & Table 1). We adopt $\Omega_a \sim 150$ m² yr⁻¹ from the top of the range, as it is based on a weaker temperature dependence (a power of 1.5) that is more consistent with the one (1.75) found across the literature on gas diffusion (e.g., Tang et al., 2014).

Now, if we focus on the top few metres of the firn and account for the relative density $\rho_0/\rho_i \sim 0.4$ there, then the diffusion coefficient for the bulk firn would be less, $\approx \Omega_a(1-\rho_0/\rho_i)$, but this correction is offset by a strong enhancement of diffusion by firn ventilation and wind pumping (e.g., Colbeck, 1989; Waddington et al., 1996). We therefore proceed by using the free-air diffusivity Ω_a without correction. A ballpark estimate of D from vapour diffusion is found by scaling Ω_a by the abundance ratio of SO_4^{2-} in the air to ice. The vapour pressure p_v converts via the ideal gas law to 2.7×10^{-12} mol m⁻³, whereas for a volcanic signal in the firn with bulk concentration peaking at 200 ppb (≈ 2 nmoles/g), the peak sulphate abundance is ≈ 2 mmol m⁻³ in the ice grains or ≈ 0.8 mmol m⁻³ in the bulk firn. The resulting abundance ratio, $\approx 3 \times 10^{-9}$, leads to the bulk diffusivity $D \sim 4.5 \times 10^{-7}$ m² yr⁻¹, similar to the shallow high values on our D(t) profile.

The assumption regarding time scales may be checked. For signals on the decimetre scale $l \sim 0.1$ m, the vapour-diffusion time scale, $l^2/D \sim 10^4$ yr, is much longer than the solid-diffusion time scale, $d_g^2/D_s \sim 400$ yr. These values are based on the mean grain diameter d_g in the upper firn at Dome C (≈ 0.1 –0.2 mm; Gay et al., 2002) and the assumption that the H₂SO₄ diffusivity within ice grains, D_s , is similar to the H₂O self-diffusivity of monocrystalline ice ($\sim 10^{-10}$ m² yr⁻¹ at –53 °C).

The vapour diffusion model also explains the steep drop of D in the range ≈ 0 –2.8 ka, because firn metamorphism reduces the porosity and seals off interconnecting airways to lower the bulk diffusivity (Calonne et al., 2022) on descent through the firn layer, and because as grain growth occurs in the firn, larger grains slow the H₂SO₄ diffusion from their interior to their surfaces, progressively limiting the bulk diffusion rate. At pore close-off ($\rho \approx 845$ kg m⁻³ at Dome C; Calonne et al., 2002) vapour diffusion terminates, and other processes must control D thereafter.

4.2 Sulphate transport below the firn-ice transition

630

635

640

645

650

Below pore close-off at EDC, signal smoothing may result from (i) solid-state diffusion within ice grains, (ii) "Gibbs—Thomson diffusion" of vein signals (Ng, 2021; i.e., diffusion of the part of sulphate bulk concentration in liquid veins due to thermodynamic interactions including the Gibbs—Thomson effect and melting-point depression by dissolved ions), (iii) diffusion through the grain-boundary network, (iv) "residual diffusion" caused by the stochastic three-dimensional motion of veins and grain boundaries carrying impurities (Ng, 2021), and any combination of these processes. We expect suppression of Gibbs—Thomson diffusion where the veins are disconnected or blocked by microparticles or dust (Ng, 2021), and suppression of residual diffusion where such particles impede grain-boundary motion (Durand et al., 2006).

In terms of how sulphate is partitioned in EDC ice across crystal lattice, grain boundaries and liquid veins, direct observations are limited to a small number of shallow ice samples, but they indicate its presence at grain boundaries and triple junctions. Barnes and Wolff (2004) analysed 6 samples in the 140–501 m depth range with scanning electron microscopy, finding sulphur at grain-boundary sites, and at triple junctions only in samples with high sulphate concentration; they suggested that the veins could carry much impurity only when the grain boundaries were saturated. Recently, Bohleber et al. (2025) used laser ablation inductively coupled plasma mass spectrometry (LA-ICP-MS) to map the abundances of S, Cl and Na at tens-of-microns resolution in samples from 281.6, 585.2 and 1000 m depth (9 ka, 27.3 ka, 64 ka), in places away with volcanic spikes. Their elemental maps show strong localisation of S at grain boundaries, with little of it in grain interiors, and no apparent trend in the partitioning with depth. They argued diffusion through grain boundaries (as well as veins) as potentially playing a key role in signal evolution. Measurements targeting triple junctions with a laser spot size of 1 µm also revealed S there, but the ablated material volumes were too small for determining whether S was concentrated at the junctions – as was found for Na and Cl – and its abundance ratio between triple junctions and grain boundaries.

If D_s , D_{vn} , D_{bn} and D_{res} symbolise the respective "component diffusivities" contributing to D from processes (i) to (iv) above, then one might regard D as their signal-partitioning weighted sum. In the following, we assess how they conspire with signal partitioning to different impurity sites to govern D(t) in $2.5 \le t \le 390$ ka, by estimating their profiles down column. For reasons given below, we evaluate D_{bn} only qualitatively.

We calculate D_s , D_{vn} and D_{res} by using published equations (Appendix C) and temperature and grain-size data from EDC as input (Fig. S1). These diffusivities increase with temperature. The Gibbs—Thomson diffusivity D_{vn} decreases with the mean grain size and sulphate bulk concentration c_B (Eq. (C2)). We calculate it for c_B from 1 μ M (the typical background concentration at EDC) to 10 μ M (order of magnitude of large volcanic peaks), noting that this range constrains a lower-bound D_{vn} because not all of c_B may reside in veins. For finding D_s and D_{vn} , empirical estimates of the molecular diffusivities of sulphate in ice single crystals and water are desired but lacking; we approximate them by the H₂O self-diffusivities in those materials.

Turning to the grain-boundary network diffusivity D_{bn} , we note that grain boundaries, each bounded by triple junctions, must form a discontinuous transport network that is interrupted repeatedly by triple junctions, where we envisage liquid veins to exist. Sulphate can diffuse within each grain boundary according to its molecular diffusivity, D_{gb} ; this is probably several orders of magnitude larger than the solid-state/lattice diffusivity, D_s (Lu et al., 2009; Ng, 2024). But on the centimetre or longer scale of signals of interest (over multiple grains), the veins intersect and strongly short-circuit the grain-boundary transport; the vein-water molecular diffusivity is several orders of magnitude above D_{gb} (Lu et al., 2009; Ng, 2024). Consequently, grain-boundary signal diffusion is inherently coupled to vein-signal diffusion. With D_{bn} representing diffusion of only the part of the bulk signal in grain boundaries, we expect $D_{bn} < D_{vn}$ because signal evolution involves sulphate diffusing along them (to and

from the veins) in series with the vein short-circuiting.² Any impurity segregation where grain boundaries meet vein apices might further limit D_{bn} . In this way, grain boundaries are slow (diffusive) extensions of the veins. Both the coupling and

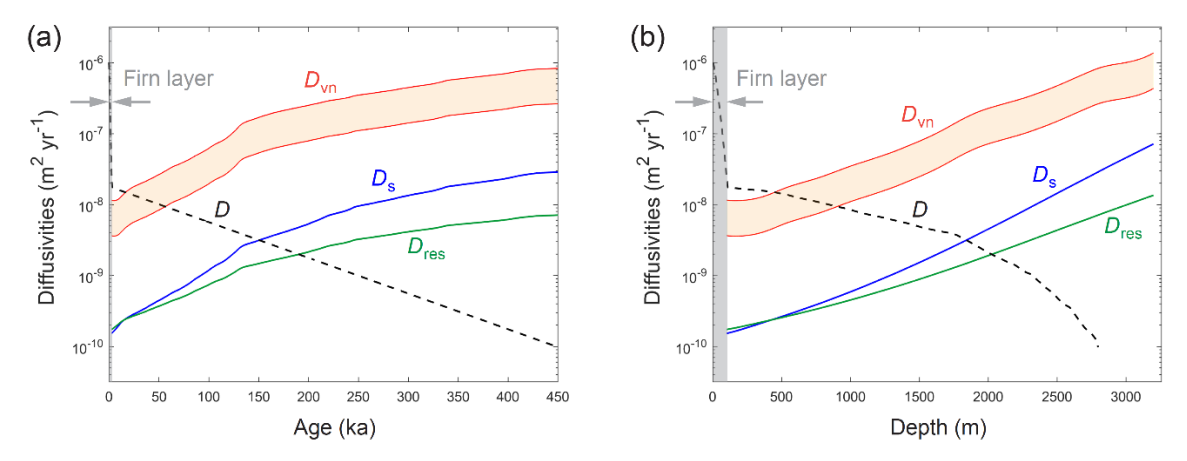


Figure 9. Estimated contributions to the sulphate signal diffusivity D in the EDC ice column (below the firn) from Gibbs—Thomson diffusion in the vein network (D_{vn}), solid-state diffusion within ice crystals (D_s), and residual diffusion (D_{res}), as functions of (a) age and (b) depth. Dashed curves plot our inversion result for D from Fig. 8b. Red shading indicates the range in D_{vn} described in the text.

segregation are poorly understood so a precise estimation of D_{bn} is presently out of reach.

685

690

695

700

Figure 9 shows the computed profiles of D_s , D_{vn} , and D_{res} , including D from Fig. 8b for comparison. D_{vn} is the highest component diffusivity. From pore close-off to ≈ 1700 m depth (≈ 130 ka), some sulphate diffusion must occur in a connected vein network because D_s and D_{res} are too small to account for D and because we expect D_{bn} to be much less than D_{vn} (possibly by one to several orders of magnitude). In the upper part of this interval, a sizeable fraction of sulphate signals must lie in veins, because the similarity of D_{vn} and D suggests that Gibbs—Thomson diffusion dominates signal smoothing, although grain-boundary diffusion in series with vein short-circuiting — as described earlier — may supplement transport. This interpretation tallies with our vapour diffusion model (Sect. 4.1), which envisages sulphuric acid present on firn grain surfaces. When the grains cross the firn-ice transition, some sulphate should end up at crystal junctions (grain boundaries and veins). Below the transition, grain boundaries may supply veins continually with sulphate, as grain growth reduces their area density. These ideas are broadly compatible with the microscale observations of Barnes and Wolff (2004) and Bohleber et al. (2025).

On descending the interval towards 1700 m, D_{vn} and D diverge (Fig. 9). Despite enhancement of D_{vn} by rising temperature (grain growth offsets this only partially, according to Eq. (C2)), D decreases. This decrease can be explained by a shift in signal

² Research on polycrystalline diffusion has also considered the effect of grain boundaries on D, but mainly for systems below the eutectic, without triple-junction melt. The focus there is different: how grain-boundary diffusion short-circuits lattice diffusion. For coupled diffusion in the long time (Harrison Type-A) regime, it is estimated that $D_{bn} \approx sfD_{gb}$, where f is the volume fraction of grain boundaries and s is the impurity segregation coefficient (e.g., Kaur et al., 1995; Dohmen & Milke, 2010). We cannot use this result when liquid veins are present.

partitioning away from veins. That is, each signal peak may be thought of generally consisting of a vein component, a grain-boundary component, and a crystal-interior component. The last component contributes minimally to signal evolution *if* we assume that the low abundance of sulphate within grains and its localisation at grain boundaries inferred by Bohleber et al. (2025) apply at all depths to 1000 m (depth of their deepest sample) and further below. As the vein component smooths by Gibbs–Thomson diffusion, the less it contributes to the peak form, so an increasing fraction of surviving signals comes from sulphate at grain boundaries, so D tends towards D_{res} and D_{bn} (note the focus on signals rather than concentration; the veins are not necessarily losing sulphate, and grain boundaries not necessarily gaining sulphate). That D has dropped to less than a tenth of D_{vn} at ≈ 1700 –2100 m suggests that by then, most vein signals have been eliminated and grain-boundary network diffusion and residual diffusion dominantly control signal smoothing. The large decrease in D through ≈ 100 –1700 m is consistent with the modelling results of Ng (2021; his Fig. 8) showing that Gibbs–Thomson diffusion rapidly damps vein sulphate signals in the upper EDC column if the veins are fully connected. In this "signal partitioning shift" mechanism, D_{vn} is unchanged from its estimated trajectory in Fig. 9 unless the veins are blocked or disconnected.

Progressive blockage of veins by dust that lowers their connectivity – and thus D_{vn} – may explain part, but not all, of the decrease in D through the interval, because Gibbs–Thomson diffusion will occur in a partially-connected vein network to cause signal partitioning shift. Consequently, signal partitioning shift with or without vein-blockage/disconnection can explain the decrease. According to R2024, vein blocking is not clearly evidenced by the EDC dust-flux record, which does not increase overall through the interval (their Fig. 5), but it cannot be ruled out while the precise microstructural distribution of dust in the ice is uncertain.

Our foregoing inferences revise the ones by R2024, who attributed the decay of D_R in 0–50 ka to a switch in diffusion mechanism due to changing location of sulphate in the microstructure and/or changing connectivity of the grain interfacial network (factors related to those identified by us above) and who interpreted the high D_R values on the decay for active diffusion through interconnected veins in ice dating to the Holocene and reaching into the last glacial. The D(t) decay analysed by us has much lower diffusivities than D_R (Fig. 8b) and extends to ≈ 130 ka, implying vein-network connectivity to greater depths. Our interpretation emphasises changing partitioning of signals (depth variations in concentration) over changing partitioning of bulk concentration (sulphate location). We also showed in Sect. 3 that the D_R decay originates from memory of very fast diffusion in the firn lasting only a few kiloyears, rather than from processes beneath the firn-ice transition.

In the $\approx 2100-2700$ m interval, D continues to plunge below $D_{\rm s}$ and $D_{\rm res}$. A plausible interpretation of this focusses on grain-boundary signals, as there is no obvious mechanism of lowering $D_{\rm s}$ substantially, and our earlier inference suggests limited vein signals surviving to these depths. The observed D may result from suppressed residual diffusion due to dust-particle drag on grain boundaries, together with grain-boundary network diffusion rates $D_{\rm bn}$ not exceeding $\sim 10^{-10}-10^{-9}$ m² yr⁻¹. As $D_{\rm bn} \ll D_{\rm s}$ then, this interpretation suggests potential bottlenecks (e.g., segregation effects) where grain boundaries connect with veins. We emphasise that our analysis for this interval does not address the deep anomalous sulphate peaks described in Sect. 1.

These inferences from order-of-magnitude comparisons in Fig. 9 are preliminary, given the approximations for the molecular diffusivities, the uncertainty with the size of D_{bn} , our use of simple models (Appendix C) that ignore other ionic impurities besides sulphate (which may impact D_{vn}) and potential anisotropy in grain-boundary motion and orientation (which may impact D_{res}) and that does not capture the coupled diffusion in grain boundaries and veins (as modelled by Ng (2024) for water stable isotopes), and given the assumptions made from the Bohleber et al. (2025) findings, which themselves are based on a few samples not carrying sulphate peak signals. Our most robust interpretation is the shift of sulphate signals away from veins and increasing dominance of grain boundaries in carrying them as we descend the upper half column.

5 Conclusions and outlook

740

755

760

In this paper, we advanced a theory of diffusivity inversion for impurity signals in ice cores and applied it to the sulphate datasets of F2024 and R2024 to estimate the diffusivity (D) profile at the EDC core site, gaining new insights on sulphate transport in the ice column there to ≈ 2700 m depth. Our framework unifies and extends the methods of F2024 and R2024 for finding the effective diffusivities (D_R , D_{F1} , D_{F2}) and reconciles their results. The effective diffusivities differ significantly from the local diffusivity D because they are nonuniform-weighted averages of D over large, finite age intervals. The "memory effect" from this averaging explains how the decay in D_R in ~ 0 –50 ka found by R2024 originates from high diffusivity in the thin (≈ 0 –100 m equating to ≈ 0 –2.5 ka) firn layer atop the column. By incorporating firn densification in the model, we show that D retrieved in the firn by the inversion measures the impurity diffusivity of bulk firn material. Our theory can be used on other ice cores and other chemical impurities to estimate the corresponding diffusivity profiles.

The EDC sulphate diffusivity profile (Fig. 8b) shows high, sharply decreasing D in the firn layer (≈ 0 –100 m depth), followed by a gradual decline from $\sim 10^{-8}$ to $\sim 10^{-10}$ m² yr⁻¹ through ≈ 110 –2700 m (≈ 2.8 –390 ka). We propose vapour diffusion of sulphuric acid in firn air as the cause of the high firn diffusivity. By studying how the profile is controlled by the component impurity transport mechanisms (i.e., diffusion through crystal lattice, veins, and grain boundaries, and residual diffusion due to interfacial motion), we interpret the decline in D in ≈ 110 –2000 m for a progressive removal of vein sulphate signals by Gibbs–Thomson diffusion, which leaves more and more of the remaining signals to grain boundaries, and the further decline in D in ≈ 2000 –2700 m for slow diffusion through the grain-boundary network and potential slowing of grain-boundary motion by dust/microparticle drag. These factors can explain why D decreases with depth despite rising temperature. Our findings broadly agree with F2024 and R2024's interpretation (from their effective diffusivities) of limited vein-signal diffusion at depth, but yield more precise and reliable information about changing signal partitioning in the upper half column.

5.1 Implications

What of the fate of sulphate signals deposited on the surface of Dome C? Our diffusivity profile implies that if they survive the initial fast diffusion in the firn layer to "punch through" to its base, then afterwards they enjoy much slower diffusive smoothing and might survive into deep ice. For sulphate signals generally, not only volcanically-sourced spikes, we study this in Fig. 10 by computing the vertical variation of diffusion length σ (using Eq. (24) with our D profile) and using σ to predict

the amplitude attenuation ratio for peak signals with annual, 3-year, decadal and centennial durations, i.e., peaks whose depositional widths at the surface are 1, 3, 10 and 100 times the mean annual layer thickness (\approx 53 mm after accounting for the surface firn density, taken as 400 kg m⁻³). The 3-year long signal is akin to the original surface peaks assumed in our inversion method, so its predicted attenuation trajectory resembles the trajectory of the α -data (Fig. 10a; cf. Fig. 4a).

770

775

780

785

790

As shown in Fig. 10, the initial rise in σ reflecting fast diffusion in the firn gives a total firn diffusion length of 3.6 cm. Annual signals attenuate drastically and struggle to punch through, although those with high starting amplitudes may remain

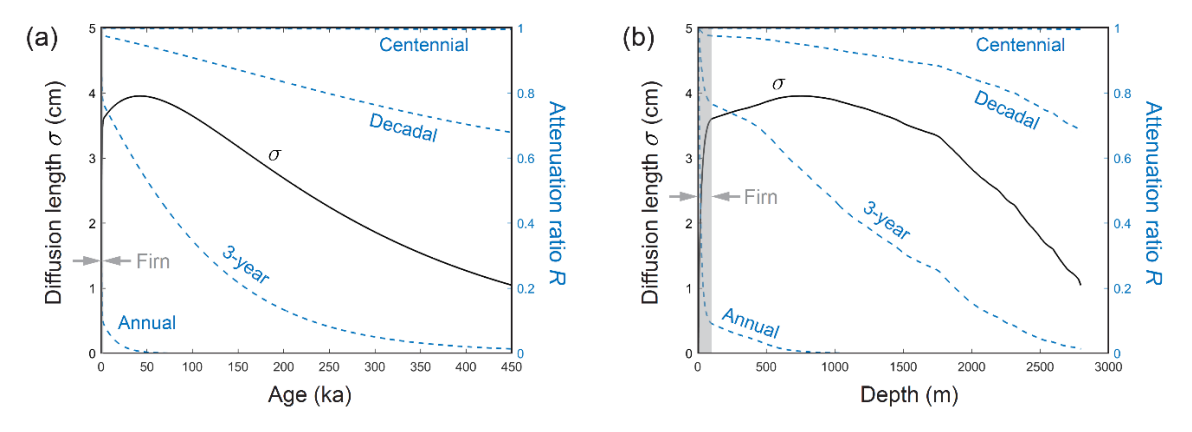


Figure 10. Diffusion length σ at the EDC core site (solid curves, left axes) against (a) age and (b) depth, calculated with Eq. (24) using the diffusivity profile D(t) from the inversion in Fig. 8b. Grey shading indicates the firn layer. Dashed curves (right axes) plot the amplitude attenuation ratio $R = \exp(-2\pi^2\sigma^2/(\lambda_0 S)^2)$ (equivalent to the right-hand side of Eq. (22)) for signal peaks that are annual, 3-year, decadal and centennial in duration. As these signals are not sinusoidal, we estimate R by approximating the wavelength λ_0 to be twice their widths.

detectable for some distance below the firn. Decadal and longer signals attenuate significantly less. The attenuation amount depends sensitively on the width of signals that are annual to decadal. Notably, since volcanic events vary widely in duration, their sulphate spikes in the ice have marginal survivability, in the sense that 3-year long spikes could reach ≈ 1500 m depth with 1/3 of their original amplitude, but slightly shorter spikes perish much faster. This means that the FIC sulphate record presents a filtered history of volcanic forcing with short (as well as low magnitude) eruptions severely underrepresented. For non-volcanic forcings, similar low-pass filtering suppresses sub-decadal signals. Note that the sulphate diffusion lengths in Fig. 10 do not apply to water stable isotopes, and, across the depth range considered here, they are less than or similar to modelled diffusion lengths for δD in the same core (Fig. 6 of Pol et al., 2010), indicating slightly better signal preservation for sulphate compared to water isotopes.

For the ongoing Beyond EPICA – Oldest Ice (BE-OI) project and the Million Year Ice Core (MYIC) project at nearby Little Dome C, a key interest is the resolution of recoverable climate signals in ice 1–1.5 Myr old. The extreme layer thinning experienced by that ice, whose age density is expected to reach 20 kyr m⁻¹ or more at 1.5 Ma (Chung et al., 2023), will limit

the retrieval and interpretation of signals of shorter than millennial time scale; e.g., centennial signals may be contained in 795 sections ~ 1 cm long, similar to individual grain diameter. Still, it is useful to know the diffusion length σ of (potentially observable) longer-scale signals. Here we estimate σ for sulphate in deep ice at Little Dome C, by assuming that the diffusivity profile there has the same form as found for EDC back to 450 ka and is, beyond that age, capped at 10⁻¹⁰ m² yr⁻¹, the value on our D-profile at 450 ka (Fig. S2). A first calculation, made by integrating Eq. (24) again but with the thinning function S(t)derived from the modelled age-depth scales at the BE-OI and MYIC core sites (Chung et al., 2023), predicts $\sigma = 0.5$ -0.9 cm 800 from 500 ka to 2 Ma (Fig. S3), with σ variations in 0-450 ka very similar to the EDC result. Separately, we then make a bounded estimate that does not depend on the age-depth scales at those sites. We use the property that the squared-diffusion lengths σ^2 from two contiguous parts of an ice column are additive after applying the respective vertical thinning (Gkinis et al., 2014; Ng, 2023). Thus, the value of σ^2 at 1.5 Ma can be found by taking σ^2 at 450 ka from Fig. 10 (where $\sigma \approx 1$ cm) and adding a σ^2 contribution from an extra 1.05 Myr (Δt) of signal diffusion at constant diffusivity 10^{-10} m² yr⁻¹; we deliberately ignore the effect of layer thinning on this contribution, taking it as $2D\Delta t$, to overestimate the total σ . This second calculation 805 conservatively constrains the maximum sulphate diffusion length to be 1.8 cm at 1.5 Ma (2 cm if made for 2 Ma).

These diffusion length results for EDC and Little Dome C (Figs. 10 and S3) pertain only to sulphate signals that entered the ice column at the top and underwent diffusion and shortening, not to signals produced or modified by other processes (e.g. the anomalous deep peaks described in Sect. 1), to which the concept of diffusion length may not apply.

Estimating the sulphate signal survival for ice-core sites outside the Dome C region is not attempted, as it requires specific knowledge about their diffusivity profiles or bolder assumptions (than for Little Dome C) to be made for those profiles.

5.2 Future research

810

815

820

The fast sulphate diffusion in EDC firn discovered by us, which has not been recognised before, motivates enquiry into its origin and a wider study at multiple locations. Inversions should be made with high-resolution sulphate records from other ice cores from Antarctica and Greenland to see if they show rapid firn diffusion, and to study the factors behind the diffusivity, e.g., temperature and accumulation rate. In some of those exercises, signal diffusion in the firn might not be apparent from visual inspection of the observed firn peaks (e.g., our EDC record features only 8 major sulphate peaks in the firn, amidst diverse background fluctuations, that do not show a clear trend of amplitude decay); then, as in our study, the peaks far below the firn layer may prove to be instrumental for constraining the firn diffusivity via the memory effect. Also, our proposed mechanism for the firn – involving both H₂SO₄ vapour diffusion in firn air and the assumed availability of sulphuric acid on grain surfaces (Sect. 4.1) – needs to be tested by in-situ chemical analysis in the field or laboratory experiments on firn samples.

The inversion and measurement results will help us model the depth variation of D in the firn at a level of sophistication like in the Whillans and Grootes (1985) isotope diffusion model.

Another avenue concerns the grain-scale mechanisms of ionic impurity transport in polycrystalline ice, which are is critical for understanding post-depositional signal alteration on ice-core records and are is a known stumbling block (Stoll et al., 2021; Ng, 2021; R2024 and F2024). Although our work in Sect. 4.2 shows that we can begin to estimate the diffusivity contributions of component transport mechanisms, the partitioning of impurity to different sites and how impurity transfer between them occurs and alters the partitioning – and thus the bulk-signal diffusivity – remain poorly understood. There is also possibility for signal modification by mechanisms involving more than just diffusion, e.g., reactions between different compounds or between dissolved ions and dust particles. It is enticing to build theoretical models for all these processes, but we need abundant microscale observations of the impurity distribution to inform the effort. For sulphate, it is hoped that the LA-ICP-MS mapping of S (Bohleber et al., 2025) will soon be used to analyse much more of the length of the EDC core with dense sampling, including stretches across peak signals. The results will yield high-resolution data on dust distribution and grain size as well, which can help us understand what governs the decay on the *D* profile and refine our interpretation in Sect. 4.2. Accurate experimental data on the low-temperature molecular diffusivities of different ions (not limited to sulphate) in monocrystalline ice, in water and at grain boundaries are also highly desirable.

A <u>separate-different</u> challenge is to extend our inversion theory to non-steady state conditions, where the vertical profiles of D and $\dot{\varepsilon}_z$ evolve with time (over glacial-interglacial time scales) as a result of climatic forcing that influences the physical properties of the ice from different periods. Such work can shed light on which of the shorter fluctuations in the effective diffusivity D_R (as discussed by R2024) reflect true diffusivity variations and how to retrieve them by inversion.

Acknowledgements

825

830

835

840

845

850

FSLN thanks the City University of Hong Kong for library facilities during research visits. EWW was supported by a Royal Society professorship for part of this study. TJF was supported by US National Science Foundation grants 2149518 (Office of Polar Programs) and 2019719 (Center for Oldest Ice Exploration, a Science and Technology Center). We acknowledge funding support from the University of Sheffield Institutional Open Access Fund for covering the publication cost. For the purpose of open access, the author has applied a Creative Commons Attribution (CC BY) licence to any Author Accepted Manuscript version arising from this submission.

Code and data availability

<u>TAll of the EDC</u> sulphate signal data used by us come from Fudge et al. (2024) and Rhodes et al. (2024). <u>Our computed results</u> in Figs. 4, 6–10, and S3 are archived at https://doi.org/10.15131/shef.data.29015291 (Ng, 2025). <u>Our study does not produce major primary datasets or simulation outputs.</u> Our modelling results are available from the first author on request.

Author contribution

FSLN formulated the theory, performed the calculations with data provided by the other authors, and wrote the manuscript.

RHR, TJF, and EWW contributed knowledge and ideas to the analyses and interpretations and helped shape the paper's messages.

Competing interests

TJF is an editorial board member of The Cryosphere.

References

- Barnes, P. R. F., Mader, H. M., Röthlisberger, R., Udisti, R., and Wolff, E. W.: The evolution of chemical peak shapes in the Dome C ice core, Antarctica, J. Geophys. Res., 108, 4126, doi:10.1029/2002JD002538, 2003.
 - Barnes, P. R. F. and Wolff, E. W.: Distribution of soluble impurities in cold glacial ice, J. Glaciol., 50, 311–324, https://doi.org/10.3189/172756504781829918, 2004.
- Bazin, L., Landais, A., Lemieux-Dudon, B., Toyé Mahamadou Kele, H., Veres, D., Parrenin, F., Martinerie, P., Ritz, C., Capron, E., Lipenkov, V., Loutre, M.-F., Raynaud, D., Vinther, B., Svensson, A., Rasmussen, S. O., Severi, M., Blunier, T., Leuenberger, M., Fischer, H., Masson-Delmotte, V., Chappellaz, J., and Wolff, E.: An optimized multi-proxy, multisite Antarctic ice and gas orbital chronology (AICC2012): 120–800 ka, Clim. Past, 9, 1715–1731, https://doi.org/10.5194/cp-9-1715-2013, 2013.
 - BE-OI: Beyond EPICA Oldest Ice, https://www.beyondepica.eu/en/ (last access: 1 March 2025), 2017.
- Bohleber, P., Stoll, N., Larkman, P., Rhodes, R. H., and Clases, D.: New evidence on the microstructural localization of sulfur, chlorine & sodium in polar ice cores with implications for impurity diffusion, EGUsphere [preprint], https://doi.org/10.5194/egusphere-2025-355, 2025.
 - Bouchet, M., Landais, A., Grisart, A., Parrenin, F., Prié, F., Jacob, R., Fourré, E., Capron, E., Raynaud, D., Lipenkov, V. Y., Loutre, M.-F., Extier, T., Svensson, A., Legrain, E., Martinerie, P., Leuenberger, M., Jiang, W., Ritterbusch, F., Lu, Z.-T., and Yang, G.-M.: The Antarctic Ice Core Chronology 2023 (AICC2023) chronological framework and associated timescale for the European Project for Ice Coring in Antarctica (EPICA) Dome C ice core, Climate of the Past, 19, 2257–2286, https://doi.org/10.5194/cp-19-2257-2023, 2023.
 - Brus, D., Škrabalová, L., Herrmann, E., Olenius, T., Trávničková, T., Makkonen, U., and Merikanto, J., 2017. Temperature-dependent diffusion of H2SO4 in air at atmospherically relevant conditions: laboratory measurements using laminar flow technique, Atmosphere, 8(7), 132, https://doi.org/10.3390/atmos8070132, 2017.

- Calonne, N., Burr, A., Philip, A. Flin, F. and Geindreau, C.: Effective coefficient of diffusion and permeability of firn at Dome C and Lock In, Antarctica, and of various snow types estimates over the 100–850 kg m⁻³ density range, The Cryosphere, 16, 967-980, https://doi.org/10.5194/tc-16-967-2022, 2022.
 - Castellano, E., Becagli, S., Jouzel, J., Migliori, A., Severi, M., Steffensen, J. P., Traversi, R., and Udisti, R.: Volcanic eruption frequency over the last 45 ky as recorded in Epica-Dome C ice core (East Antarctica) and its relationship with climatic changes, Global Planet. Change, 42, 195–205, https://doi.org/10.1016/j.gloplacha.2003.11.007, 2004.
 - Chung, A., Parrenin, F., Steinhage, D., Mulvaney, R., Martín, C., Cavitte, M. G. P., Lilien, D. A., Helm, V., Taylor, D., Gogineni, P., Ritz, C., Frezzotti, M., O'Neill, C., Miller, H., Dahl-Jensen, D., and Eisen, O.: Stagnant ice and age modelling in the Dome C region, Antarctica, The Cryosphere, 17, 3461–3483, https://doi.org/10.5194/tc-17-3461-2023, 2023.
 - Colbeck, S. C.: Air movement in snow due to windpumping, J. Glaciol., 35, 209-213, 1989.

- Dohmen, R. and Milke R.: Diffusion in polycrystalline materials: grain boundaries, mathematical models, and experimental data, Rev. Mineral. Geochem., 72(1), 921–970, https://doi.org/10.2138/rmg.2010.72.21, 2010.
 - Durand, G., Weiss, J., Lipenkov, V., Barnola, J., Krinner, G., Parrenin, F., Delmonte, B., Ritz, C., Duval, P., Röthlisberger, R., and Bigler, M.: Effect of impurities on grain growth in cold ice sheets, J. Geophys. Res.-Earth, 111, F01015, https://doi.org/10.1029/2005JF000320, 2006.
- 895 EPICA community members: Eight glacial cycles from an Antarctic ice core, Nature, 429, 623–628, https://doi.org/10.1038/nature02599, 2004.
 - Fudge, T. J., Sauvage, R., Vu, L., Hills, B. H., Severi, M., and Waddington, E. D.: Effective diffusivity of sulfuric acid in Antarctic ice cores, Clim. Past, 20, 297–312, https://doi.org/10.5194/cp-20-297-2024, 2024.
- Gay, M., Fily, M., Genthon, C., Frezotti, M., Oerter, H., and Winther, J.-G.: Snow grain size measurements in Antarctica, J. Glaciol., 48(163), 527–535, https://doi.org/10.3189/172756502781831016, 2002.
 - Gkinis, V., Simonsen, S. B., Buchardt, S. L., White, J. W. C, and Vinther, B. M.: Water isotope diffusion rates from the NorthGRIP ice core for the last 16,000 years Glaciological and paleoclimatic implications, Earth Planet. Sci. Lett., 405, 132–141, https://doi.org/10.1016/j.epsl.2014.08.022, 2014.
- Johnsen, S. J.: Stable isotope homogenization of polar firn and ice. International Association of Hydrological Sciences

 Publication 118 (Symposium at Grenoble 1975: Isotopes and Impurities in Snow and Ice), 210–219, 1977.
 - Kaur, I., Mishin, Y., and Gust, W.: Fundamentals of grain and interphase boundary diffusion, 3rd edition, John Wiley & Sons, New York, 513 pp., ISBN 047193819X, 1995.
- Landais, A., Barnola, J. M., Kawamura, K., Caillon, N., Delmotte, M., Van Ommen, T., Dreyfus, G., Jouzel, J., Masson-Delmotte, V., Minster, B., Freitag, J., Leuenberger, M., Schwander, J., Huber, C., Etheridge, D., and Morgan, V.: Firn-air δ15N in modern polar sites and glacial-interglacial ice: a model-data mismatch during glacial periods in Antarctica?, Quat. Sci. Rev., 25, 49–62, https://doi.org/10.1016/j.quascirev.2005.06.007, 2006.
 - Legrand, M. and Mayewski, P.: Glaciochemistry of polar ice cores: a review, Rev. Geophys., 35, 219–243, https://doi.org/10.1029/96RG03527, 1997.

- Lin, J., Svensson, A., Hvidberg, C. S., Lohmann, J., Kristiansen, S., Dahl-Jensen, D., Steffensen, J. P., Rasmussen, S. O.,
 Cook, E., Kjær, H. A., Vinther, B. M., Fischer, H., Stocker, T., Sigl, M., Bigler, M., Severi, M., Traversi, R., and Mulvaney,
 R.: Magnitude, frequency and climate forcing of global volcanism during the last glacial period as seen in Greenland and
 Antarctic ice cores (60–9 ka), Clim. Past, 18, 485–506, https://doi.org/10.5194/cp-18-485-2022, 2022.
 - Lu, H., McCartney, S. A., and Sadtchenko, V.: H/D exchange kinetics in pure and HCl doped polycrystalline ice at temperatures near its melting point: Structure, chemical transport, and phase transitions at grain boundaries, J. Chem. Phys., 130, 054501, https://doi.org/10.1063/1.3039077, 2009.
 - Mader, H. M.: The thermal behaviour of the water-vein system in polycrystalline ice, J. Glaciol., 38, 359–374, 1992.

- Mulvaney, R., Wolff, E. W., and Oates, K.: Sulphuric acid at grain boundaries in Antarctic ice, Nature, 331, 247-249, 1988.
- MYIC: Million Year Ice Core, https://www.antarctica.gov.au/science/climate-processes-and-change/antarctic-palaeoclimate/million-year-ice-core/ (last access: 1 March 2025), 2020.
- 925 Ng, F. S. L.: Pervasive diffusion of climate signals recorded in ice-vein ionic impurities, The Cryosphere, 15, 1787–1810, https://doi.org/10.5194/tc-15-1787-2021, 2021.
 - Ng, F. S. L.: Isotopic diffusion in ice enhanced by vein-water flow, The Cryosphere, 17, 3063–3082, https://doi.org/10.5194/tc-17-3063-2023, 2023.
 - Ng, F. S. L.: The grain-scale signature of isotopic diffusion in ice, The Cryosphere, 18, 4645–4669, https://doi.org/10.5194/tc-18-4645-2024, 2024.
 - Ng, F. S. L.: Modelling results of the study "Doomed descent? How fast sulphate signals diffuse in the EPICA Dome C ice column", University of Sheffield [data set], https://doi.org/10.15131/shef.data.29015291, 2025.
 - Nye, J. F.: The geometry of water veins and nodes in polycrystalline ice, J. Glaciol., 35, 17–22, 1989.
- Pol, K., Masson-Delmotte, V., Johnsen, S., Bigler, M., Cattani, O., Durand, G., Falourd, S., Jouzel, J., Minster, B., Parrenin, F., Ritz, C., Steen-Larsen, H. C., and Stenni, B.: New MIS 19 EPICA Dome C high resolution deuterium data: Hints for a problematic preservation of climate variability at sub-millennial scale in the "oldest ice", Earth Planet. Sc. Lett., 298, 95–103, https://doi.org/10.1016/j.epsl.2010.07.030, 2010.
 - Ramseier, R. O.: Self-diffusion of tritium in natural and synthetic ice monocrystals, J. Appl. Phys., 38, 2553–2556, 1967.
- Rhodes, R. H., Bollet-Quivogne, Y., Barnes, P., Severi, M., and Wolff, E. W.: New estimates of sulfate diffusion rates in the EPICA Dome C ice core, Clim. Past, 20, 2031–2043, https://doi.org/10.5194/cp-20-2031-2024, 2024.
 - Severi, M., Udisti, R., Becagli, S., Stenni, B., and Traversi, R.: Volcanic synchronisation of the EPICA-DC and TALDICE ice cores for the last 42 kyr BP, Clim. Past, 8, 509–517, https://doi.org/10.5194/cp-8-509-2012, 2012.
 - Stoll, N., Eichler, J., Hörhold, M., Shigeyama, W., and Weikusat, I.: A review of the microstructural location of impurities in polar ice and their impacts on deformation, Front. Earth Sci. 8:615613, doi: 10.3389/feart.2020.615613, 2021.
- 945 Svensson, A., Dahl-Jensen, D., Steffensen, J. P., Blunier, T., Rasmussen, S. O., Vinther, B. M., Vallelonga, P., Capron, E., Gkinis, V., Cook, E., Kjær, H. A., Muscheler, R., Kipfstuhl, S., Wilhelms, F., Stocker, T. F., Fischer, H., Adolphi, F., Erhardt, T., Sigl, M., Landais, A., Parrenin, F., Buizert, C., McConnell, J. R., Severi, M., Mulvaney, R., and Bigler, M.:

- Bipolar volcanic synchronization of abrupt climate change in Greenland and Antarctic ice cores during the last glacial period, Clim. Past, 16, 1565–1580, https://doi.org/10.5194/cp-16-1565-2020, 2020.
- 950 Tang, M. J., Cox, R. A., and Kalberer, M.: Compilation and evaluation of gas phase diffusion coefficients of reactive trace gases in the atmosphere: volume 1. Inorganic compounds, Atmos. Chem. Phys., 14(17), 9233–9247, https://doi.org/10.5194/acp-14-9233-2014, 2014.

- Traversi, R., Becagli, S., Castellano, E., Migliori, A., Severi, M., and Udisti, R.: High-resolution fast ion chromatography (FIC) measurements of chloride, nitrate and sulphate along the EPICA Dome C ice core. Ann. Glaciol., 35, 291–298, https://doi.org/10.3189/172756402781816564, 2002.
- Traversi, R., Becagli, S., Castellano, E., Marino, F., Rugi, F., Severi, M., de Angelis, M., Fischer, H., Hansson, M., Stauffer, B., Steffensen, J. P., Bigler, M., and Udisti, R.: Sulfate spikes in the deep layers of EPICA-Dome C ice core: Evidence of glaciological artifacts, Environ. Sci. Technol., 43, 8737–8743, doi:10.1021/es901426y, 2009.
- Tsagkogeorgas, G., Roldin, P., Duplissy, J., Rondo, L., Tröstl, J., Slowik, J. G., Ehrhart, S., Franchin, A., Kürten, A., Amorim,
 A., Bianchi, F., Kirkby, J., Petäjä, T., Baltensperger, U., Boy, M., Curtius, J., Flagan, R. C., Kulmala, M., Donahue, N. M.,
 and Stratmann, F.: Evaporation of sulfate aerosols at low relative humidity, Atmos. Chem. Phys., 17, 8923–8938,
 https://doi.org/10.5194/acp-17-8923-2017, 2017.
 - Umino, S. and Newman, J.: Temperature dependence of the diffusion coefficient of sulfuric acid in water, J. Electrochem. Soc., 144, 1302–1307, 1997.
- Veres, D., Bazin, L., Landais, A., Toyé Mahamadou Kele, H., Lemieux-Dudon, B., Parrenin, F., Martinerie, P., Blayo, E., Blunier, T., Capron, E., Chappellaz, J., Rasmussen, S. O., Severi, M., Svensson, A., Vinther, B., and Wolff, E. W.: The Antarctic ice core chronology (AICC2012): an optimized multi-parameter and multi-site dating approach for the last 120 thousand years, Clim. Past, 9, 1733–1748, https://doi.org/10.5194/cp-9-1733-2013, 2013.
- Waddington, E. D., Cunningham, J., and Harder, S. L.: The effects of snow ventilation on chemical concentrations, in:

 Chemical exchange between the atmosphere and polar snow, edited by Wolff, E. W. and Bales, R. C., NATO ASI series,

 Series 1, Vol. 43, Springer, Berlin, Heidelberg, Germany, 403–451, https://doi.org/10.1007/978-3-642-61171-1, 1996.
 - Whillans, I. M. and Grootes, P. M: Isotopic diffusion in cold snow and firn, J. Geophys. Res., 90(D2), 3910–3918, https://doi.org/10.1029/JD090iD02p03910, 1985.
 - Wolff, E. W., Mulvaney, R., and Oates, K.: The location of impurities in Antarctic ice. Ann. Glaciol., 11, 194–197, 1988.
- Wolff, E. W., Burke, A., Crick, L., Doyle, E. A., Innes, H. M., Mahony, S. H., Rae, J. W. B., Severi, M., and Sparks, R. S. J.: Frequency of large volcanic eruptions over the past 200 000 years, Clim. Past, 19, 23–33, https://doi.org/10.5194/cp-19-23-2023, 2023.

Appendix A

980 Table A1: Key mathematical symbols in our model.

a Ice-equivalent accumulation rate (m/yr) c B Impurity bulk concentration (amount per volume), i.e., c B = ρ C C Impurity bulk concentration (μ g kg ⁻¹ , or μ g L ⁻¹ of meltwater) d_g Mean grain diameter D Local or true diffusivity of sulphate signals (m ² yr ⁻¹) D_{bm} Signal diffusivity in the grain-boundary network D_c Corner diffusivity value on $D(t)$ profile D_{eff} Effective diffusivity D_g Molecular diffusivity from signal-gradient based inversion (corrected value) D_F Effective diffusivity from signal-gradient based inversion (barnes et al., 2003) D_F Effective diffusivity from signal-gradient based inversion (Barnes et al., 2003) D_F Effective diffusivity from signal-gradient based inversion (Barnes et al., 2003) D_F Effective diffusivity from peak-amplitude based inversion (Barnes et al., 2003) D_F Effective diffusivity from signal-gradient based inversion (Barnes et al., 2003) D_F Effective diffusivity from peak-amplitude based inversion (Barnes et al., 2003) D_F Effective diffusivity from signal-gradient based inversion D_F Solid-state diffusivity from stochastic motion of veins and gra		
C Impurity bulk concentration (μ g kg ⁻¹ , or μ g L ⁻¹ of meltwater) d_g Mean grain diameter D Local or true diffusivity of sulphate signals (m ² yr ⁻¹) D_{bm} Signal diffusivity in the grain-boundary network D_c Corner diffusivity value on $D(t)$ profile D_{eff} Effective diffusivity D_g Molecular diffusivity from signal-gradient based inversion (corrected value) D_F Effective diffusivity from peak-width based inversion (Barnes et al., 2003) D_R Effective diffusivity from signal-gradient based inversion (Barnes et al., 2003) D_R Effective diffusivity from peak-amplitude based inversion D_R Residual diffusivity from stochastic motion of veins and grain boundaries D_S Solid-state diffusivity in ice grains D_{vm} Diffusivity of vein impurity signals ("Gibbs-Thomson diffusivity") k^* Signal wavenumber \overline{m} Signal mean absolute gradient p_V H2SO4 vapour pressure in firm air S Thinning factor in the ice column t_c Corner age value on $D(t)$ profile U Firm velocity vector, = (U, V, W) W Mean destrained wavelength o	nulat	lation rate (m/yr)
Mean grain diameter D Local or true diffusivity of sulphate signals ($m^2 \text{ yr}^{-1}$) D_{bn} Signal diffusivity in the grain-boundary network D_c Corner diffusivity value on $D(t)$ profile D_{eff} Effective diffusivity D_gb Molecular diffusivity i grain boundaries D_E Effective diffusivity from signal-gradient based inversion (corrected value) D_{F1} Effective diffusivity from peak-width based inversion D_{F2} Effective diffusivity from signal-gradient based inversion (Barnes et al., 2003) D_R Effective diffusivity from peak-amplitude based inversion D_{res} Residual diffusivity from stochastic motion of veins and grain boundaries D_s Solid-state diffusivity in ice grains D_{vn} Diffusivity of vein impurity signals ("Gibbs-Thomson diffusivity") k^* Signal wavenumber \bar{m} Signal mean absolute gradient p_v H ₂ SO ₄ vapour pressure in firm air D_s Thinning factor in the ice column D_s Age D_s Corner age value on $D(t)$ profile D_s Wean destrained wavelength of signals D_s Depth below a material horizon D_s Relative signal peak amplitude (ratio of observed amplitude to reconstructed amp D_s Relative signal peak width (ratio of observed width to original width) D_s Vertical strain rate D_s Depth in the interval which the lates of the constructed width to original width)	ıtrat	ation (amount per volume), i.e., $c_B = \rho C$
Local or true diffusivity of sulphate signals (m² yr¹) D_{bn} Signal diffusivity in the grain-boundary network D_{c} Corner diffusivity value on $D(t)$ profile D_{eff} Effective diffusivity D_{gb} Molecular diffusivity i grain boundaries D_{E} Effective diffusivity from signal-gradient based inversion (corrected value) D_{F1} Effective diffusivity from peak-width based inversion D_{F2} Effective diffusivity from peak-amplitude based inversion D_{F3} Residual diffusivity from stochastic motion of veins and grain boundaries D_{F4} Solid-state diffusivity in ice grains D_{F5} Solid-state diffusivity sin just ("Gibbs-Thomson diffusivity") k^* Signal wavenumber \bar{m} Signal mean absolute gradient p_{V} H2SO4 vapour pressure in firn air	ıtrat	ation ($\mu g kg^{-1}$, or $\mu g L^{-1}$ of meltwater)
D_{bn} Signal diffusivity in the grain-boundary network D_c Corner diffusivity value on $D(t)$ profile D_{eff} Effective diffusivity i grain boundaries D_E Effective diffusivity from signal-gradient based inversion (corrected value) D_F Effective diffusivity from peak-width based inversion (Barnes et al., 2003) D_F Effective diffusivity from signal-gradient based inversion (Barnes et al., 2003) D_R Effective diffusivity from peak-amplitude based inversion D_{res} Residual diffusivity from stochastic motion of veins and grain boundaries D_s Solid-state diffusivity in ice grains D_{vn} Diffusivity of vein impurity signals ("Gibbs—Thomson diffusivity") k^* Signal wavenumber \bar{m} Signal mean absolute gradient p_V H_2SO_4 vapour pressure in firn air S Thinning factor in the ice column t Age t_c Corner age value on $D(t)$ profile U Firn velocity vector, = (U, V, W) \bar{W} Mean destrained wavelength of signals z Depth below a material horizon z Depth below the ice-sheet surface α Relative signal peak amplitude (ratio of observed amplitude to reconstructed amp s Relative signal peak width (ratio of observed width to original width) s Vertical strain rateDetermined as authinged thickness.		
D_c Corner diffusivity value on $D(t)$ profile D_{eff} Effective diffusivity i grain boundaries D_E Effective diffusivity from signal-gradient based inversion (corrected value) D_F 1 Effective diffusivity from signal-gradient based inversion D_{F2} Effective diffusivity from signal-gradient based inversion (Barnes et al., 2003) D_R Effective diffusivity from signal-gradient based inversion D_R Residual diffusivity from stochastic motion of veins and grain boundaries D_S Solid-state diffusivity in ice grains D_V n Diffusivity of vein impurity signals ("Gibbs—Thomson diffusivity") k^* Signal wavenumber \overline{m} Signal mean absolute gradient p_V H_2SO_4 vapour pressure in firm air S Thinning factor in the ice column t Age t_c Corner age value on $D(t)$ profile U Firm velocity vector, = (U, V, W) \overline{w} Mean destrained wavelength of signals z Depth below a material horizon z Depth below the ice-sheet surface z Relative signal peak amplitude (ratio of o	ity	y of sulphate signals (m ² yr ⁻¹)
Define the diffusivity of the polar time of t	the g	e grain-boundary network
D_{gb} Molecular diffusivity i grain boundaries D_{E} Effective diffusivity from signal-gradient based inversion (corrected value) D_{F1} Effective diffusivity from peak-width based inversion (Barnes et al., 2003) D_{F2} Effective diffusivity from signal-gradient based inversion (Barnes et al., 2003) D_{R} Effective diffusivity from peak-amplitude based inversion D_{res} Residual diffusivity from stochastic motion of veins and grain boundaries D_{s} Solid-state diffusivity in ice grains D_{vn} Diffusivity of vein impurity signals ("Gibbs-Thomson diffusivity") k^* Signal wavenumber \overline{m} Signal mean absolute gradient p_v H_2SO_4 vapour pressure in firn air S Thinning factor in the ice column t Age t_c Corner age value on $D(t)$ profile U Firn velocity vector, = (U, V, W) \overline{w} Mean destrained wavelength of signals z Depth below a material horizon Z Depth below the ice-sheet surface α Relative signal peak amplitude (ratio of observed amplitude to reconstructed amp β Relative signal peak width (ratio of observed width to original width) $\dot{\varepsilon}_z$ Vertical strain rate	lue	e on $D(t)$ profile
Effective diffusivity from signal-gradient based inversion (corrected value) D_{F1} Effective diffusivity from peak-width based inversion D_{F2} Effective diffusivity from signal-gradient based inversion (Barnes et al., 2003) D_{R} Effective diffusivity from peak-amplitude based inversion D_{res} Residual diffusivity from stochastic motion of veins and grain boundaries D_{s} Solid-state diffusivity in ice grains D_{vn} Diffusivity of vein impurity signals ("Gibbs-Thomson diffusivity") k^* Signal wavenumber \bar{m} Signal mean absolute gradient p_{v} H ₂ SO ₄ vapour pressure in firn air S Thinning factor in the ice column t Age t_{c} Corner age value on $D(t)$ profile t Firn velocity vector, = (U, V, W) t Mean destrained wavelength of signals t Depth below a material horizon t Depth below the ice-sheet surface t Relative signal peak amplitude (ratio of observed amplitude to reconstructed amp t Relative signal peak width (ratio of observed width to original width) t Vertical strain rate		
D_{F1} Effective diffusivity from peak-width based inversion D_{F2} Effective diffusivity from signal-gradient based inversion (Barnes et al., 2003) D_R Effective diffusivity from peak-amplitude based inversion D_{res} Residual diffusivity from stochastic motion of veins and grain boundaries D_s Solid-state diffusivity in ice grains D_{vn} Diffusivity of vein impurity signals ("Gibbs-Thomson diffusivity") k^* Signal wavenumber \bar{m} Signal mean absolute gradient p_v H_2SO_4 vapour pressure in firn air S Thinning factor in the ice column t Age t_c Corner age value on $D(t)$ profile U Firn velocity vector, = (U, V, W) \bar{w} Mean destrained wavelength of signals z Depth below a material horizon Z Depth below the ice-sheet surface α Relative signal peak amplitude (ratio of observed amplitude to reconstructed amp β Relative signal peak width (ratio of observed width to original width) $\dot{\varepsilon}_z$ Vertical strain rateDestroired on with input thickness	i gı	grain boundaries
Effective diffusivity from signal-gradient based inversion (Barnes et al., 2003) D_R Effective diffusivity from peak-amplitude based inversion D_{res} Residual diffusivity from stochastic motion of veins and grain boundaries D_s Solid-state diffusivity in ice grains D_{vn} Diffusivity of vein impurity signals ("Gibbs—Thomson diffusivity") k^* Signal wavenumber \overline{m} Signal mean absolute gradient p_V H2SO4 vapour pressure in firn air S Thinning factor in the ice column t Age t_c Corner age value on $D(t)$ profile t Firn velocity vector, = (U, V, W) \overline{w} Mean destrained wavelength of signals t Depth below a material horizon t Depth below the ice-sheet surface t Relative signal peak amplitude (ratio of observed amplitude to reconstructed amp t Relative signal peak width (ratio of observed width to original width) t Vertical strain rate	fron	om signal-gradient based inversion (corrected value)
D_R Effective diffusivity from peak-amplitude based inversion D_{res} Residual diffusivity from stochastic motion of veins and grain boundaries D_s Solid-state diffusivity in ice grains D_{vn} Diffusivity of vein impurity signals ("Gibbs—Thomson diffusivity") k^* Signal wavenumber \bar{m} Signal mean absolute gradient p_v H_2SO_4 vapour pressure in firn air S Thinning factor in the ice column t Age t_c Corner age value on $D(t)$ profile U Firn velocity vector, = (U, V, W) \overline{w} Mean destrained wavelength of signals z Depth below a material horizon Z Depth below the ice-sheet surface α Relative signal peak amplitude (ratio of observed amplitude to reconstructed amp β Relative signal peak width (ratio of observed width to original width) $\dot{\varepsilon}_z$ Vertical strain rate Postericed or with install thickness.	fron	om peak-width based inversion
D_{res} Residual diffusivity from stochastic motion of veins and grain boundaries D_s Solid-state diffusivity in ice grains D_{vn} Diffusivity of vein impurity signals ("Gibbs—Thomson diffusivity") k^* Signal wavenumber \bar{m} Signal mean absolute gradient p_v H_2SO_4 vapour pressure in firn air S Thinning factor in the ice column t Age t_c Corner age value on $D(t)$ profile U Firn velocity vector, = (U, V, W) \overline{w} Mean destrained wavelength of signals z Depth below a material horizon Z Depth below the ice-sheet surface α Relative signal peak amplitude (ratio of observed amplitude to reconstructed amp β Relative signal peak width (ratio of observed width to original width) $\dot{\varepsilon}_z$ Vertical strain rate Destrained or authorized thickness	fron	om signal-gradient based inversion (Barnes et al., 2003)
D_s Solid-state diffusivity in ice grains D_{vn} Diffusivity of vein impurity signals ("Gibbs—Thomson diffusivity") k^* Signal wavenumber \bar{m} Signal mean absolute gradient p_v H_2SO_4 vapour pressure in firn air S Thinning factor in the ice column t Age t_c Corner age value on $D(t)$ profile U Firn velocity vector, = (U, V, W) \overline{w} Mean destrained wavelength of signals z Depth below a material horizon Z Depth below the ice-sheet surface α Relative signal peak amplitude (ratio of observed amplitude to reconstructed amp β Relative signal peak width (ratio of observed width to original width) $\dot{\varepsilon}_z$ Vertical strain rate Posteriord or wetkinged thickness	fron	om peak-amplitude based inversion
D_{vn} Diffusivity of vein impurity signals ("Gibbs-Thomson diffusivity") k^* Signal wavenumber \bar{m} Signal mean absolute gradient p_v H_2SO_4 vapour pressure in firn air S Thinning factor in the ice column t Age t_c Corner age value on $D(t)$ profile U Firn velocity vector, = (U, V, W) \overline{w} Mean destrained wavelength of signals z Depth below a material horizon Z Depth below the ice-sheet surface α Relative signal peak amplitude (ratio of observed amplitude to reconstructed amp β Relative signal peak width (ratio of observed width to original width) $\dot{\varepsilon}_z$ Vertical strain rate Destrained on withinged thickness.	rom	om stochastic motion of veins and grain boundaries
k^* Signal wavenumber \bar{m} Signal mean absolute gradient p_v H_2SO_4 vapour pressure in firn air S Thinning factor in the ice column t Age t_c Corner age value on $D(t)$ profile U Firn velocity vector, = (U, V, W) \bar{w} Mean destrained wavelength of signals z Depth below a material horizon Z Depth below the ice-sheet surface α Relative signal peak amplitude (ratio of observed amplitude to reconstructed amp β Relative signal peak width (ratio of observed width to original width) $\dot{\varepsilon}_z$ Vertical strain rate Posterined or unthinsed thickness	y in	n ice grains
\overline{m} Signal mean absolute gradient p_V H_2SO_4 vapour pressure in firn air S Thinning factor in the ice column t Age t_c Corner age value on $D(t)$ profile U Firn velocity vector, = (U, V, W) \overline{w} Mean destrained wavelength of signals z Depth below a material horizon Z Depth below the ice-sheet surface α Relative signal peak amplitude (ratio of observed amplitude to reconstructed amples amplitude (ratio of observed width to original width) $\dot{\varepsilon}_z$ Vertical strain rate Destrained on authings of thickness	npuı	ourity signals ("Gibbs-Thomson diffusivity")
p_{V} H ₂ SO ₄ vapour pressure in firn air S Thinning factor in the ice column t Age t_{c} Corner age value on $D(t)$ profile U Firn velocity vector, = (U, V, W) \overline{W} Mean destrained wavelength of signals z Depth below a material horizon Z Depth below the ice-sheet surface α Relative signal peak amplitude (ratio of observed amplitude to reconstructed amp β Relative signal peak width (ratio of observed width to original width) $\dot{\varepsilon}_{z}$ Vertical strain rate		
Thinning factor in the ice column t Age t_c Corner age value on $D(t)$ profile U Firn velocity vector, = (U, V, W) \overline{W} Mean destrained wavelength of signals z Depth below a material horizon z Depth below the ice-sheet surface Relative signal peak amplitude (ratio of observed amplitude to reconstructed amp z Relative signal peak width (ratio of observed width to original width) $\dot{\varepsilon}_z$ Vertical strain rate	e gra	radient
t Age t_c Corner age value on $D(t)$ profile U Firn velocity vector, = (U, V, W) \overline{W} Mean destrained wavelength of signals z Depth below a material horizon Z Depth below the ice-sheet surface α Relative signal peak amplitude (ratio of observed amplitude to reconstructed amp β Relative signal peak width (ratio of observed width to original width) $\dot{\varepsilon}_z$ Vertical strain rate	ıre iı	in firn air
t_c Corner age value on $D(t)$ profile U Firn velocity vector, = (U, V, W) \overline{W} Mean destrained wavelength of signals z Depth below a material horizon Z Depth below the ice-sheet surface α Relative signal peak amplitude (ratio of observed amplitude to reconstructed amp β Relative signal peak width (ratio of observed width to original width) $\dot{\varepsilon}_z$ Vertical strain rate Destrained on unthinned thickness	e ice	ce column
U Firm velocity vector, = (U, V, W) \overline{W} Mean destrained wavelength of signals z Depth below a material horizon Z Depth below the ice-sheet surface α Relative signal peak amplitude (ratio of observed amplitude to reconstructed amp β Relative signal peak width (ratio of observed width to original width) $\dot{\varepsilon}_z$ Vertical strain rate Destrained on authorizon		
\overline{w} Mean destrained wavelength of signals z Depth below a material horizon Z Depth below the ice-sheet surface α Relative signal peak amplitude (ratio of observed amplitude to reconstructed amp β Relative signal peak width (ratio of observed width to original width) $\dot{\varepsilon}_z$ Vertical strain rate Destrained on withinsed thickness.	D(t)	(t) profile
z Depth below a material horizon Z Depth below the ice-sheet surface α Relative signal peak amplitude (ratio of observed amplitude to reconstructed amp β Relative signal peak width (ratio of observed width to original width) $\dot{\varepsilon}_z$ Vertical strain rate Destrained on unthinned thickness	=(l	(U, V, W)
z Depth below a material horizon Z Depth below the ice-sheet surface α Relative signal peak amplitude (ratio of observed amplitude to reconstructed amp β Relative signal peak width (ratio of observed width to original width) $\dot{\varepsilon}_z$ Vertical strain rate Destrained on unthinned thickness	eler	ength of signals
α Relative signal peak amplitude (ratio of observed amplitude to reconstructed amplitude) β Relative signal peak width (ratio of observed width to original width) $\dot{\varepsilon}_z$ Vertical strain rate	ial h	l horizon
β Relative signal peak width (ratio of observed width to original width) $\dot{\varepsilon}_z$ Vertical strain rate	shee	eet surface
Relative signal peak width (ratio of observed width to original width) $\dot{\varepsilon}_z \hspace{1cm} \text{Vertical strain rate}$	amp	aplitude (ratio of observed amplitude to reconstructed amplitude
$\dot{arepsilon}_z$ Vertical strain rate	_	
Destroined or unthinned this lenge		·
7	ned	d thickness
η Variable of integration		

ho	Firn density (surface value ρ_0 , where $\rho_0/\rho_i \sim 0.4$)
$ ho_{ m i}$	Ice density (917 kg m ⁻³)
σ	Standard deviation of Gaussian signal or Johnsen's (1977) diffusion length
au	Transformed variable in Sect. 2 (proxy of age or time)
ψ	Dilated age
$\Omega_{ m a}$	H ₂ SO ₄ diffusion coefficient in firn air

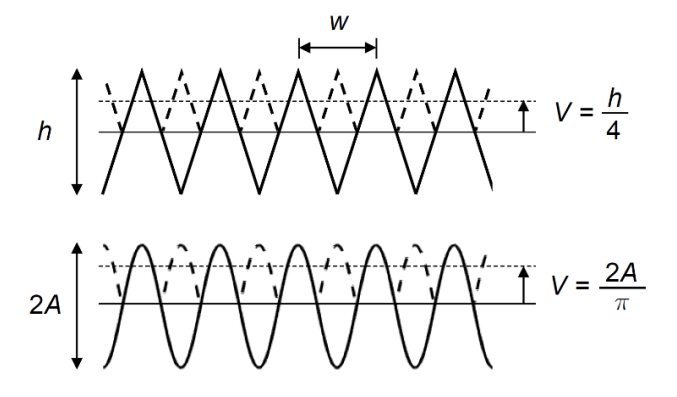
Appendix B: Estimating the wavenumber k^*

990

Barnes et al.'s (2003) formula for k^* uses the mean absolute variation V of the demeaned, preprocessed and unthinned signal:

985
$$V = \frac{1}{L} \sum_{i=1}^{n} |C_{p,i} - \bar{C}_p| \Delta \zeta$$
 (B1)

For a triangular signal of height h (Fig. B1), they state the result in Eq. (31), which is equivalent to $\overline{w}=4V/\overline{m}$, where \overline{w} is the (mean) signal wavelength. Then they calculate the wavenumber with $k^*=2\pi/\overline{w}$. In contrast, our study of this signal gives V=h/4 and mean absolute gradient $\overline{m}=2h/\overline{w}$ and hence a different result: $\overline{w}=8V/\overline{m}$ — this finding holds also for an asymmetric triangular signal. A sinusoidal signal may also be considered, e.g. $A\sin(2\pi\zeta/\overline{w})$ (Fig. B1). In this case, we find $V=2A/\pi$ and $\overline{m}=(2\pi A/\overline{w})|\cos(2\pi\zeta/\overline{w})|=4A/\overline{w}$, so $\overline{w}=2\pi V/\overline{m}$. Consequently, Barnes et al.'s \overline{w} is too small — and their k^* too large — by 2 times for a triangular signal and $\pi/2$ times for a sinusoidal signal. Real signals are typically non-periodic and different from these idealised waveforms, so k^* is overestimated by $\approx 1.57-2$ times and $D_{\rm eff}$ underestimated by $\approx 2.47-4$ times in the Barnes et al. (2003) method.



1010

1015

1020

Appendix C: Models of solid-state diffusivity D_s , vein-signal diffusivity D_{vn} , and residual diffusivity D_{res}

The sulphate diffusivity in monocrystalline ice has not been determined experimentally, as far as our literature search suggests.

As described in the text, we approximate it by the H₂O self-diffusivity in monocrystalline ice and use Ramseier's (1967) empirical formula,

$$D_{\rm s} = 9.1 \times 10^{-4} \exp\left(-\frac{7.2 \times 10^3}{T}\right) \text{ m}^2 \text{ s}^{-1}, \tag{C1}$$

where *T* is temperature in Kelvin. F2024 referred to the same approximation when qualitatively comparing their effective diffusivities to the solid-state diffusivity.

According to Eq. (23) of Ng (2021), the bulk diffusivity of ionic signals in a connected vein network in ice is given by

$$D_{\rm vn} = \frac{D_l \gamma T_0}{6\rho_i L d_{\rm o}} \sqrt{\frac{3\alpha_0}{c_{\rm R} \Gamma(T_0 - T)}},\tag{C2}$$

where D_l is the sulphate molecular diffusivity in water, c_B is the sulphate bulk concentration (by volume) in the ice, and d_g is the mean grain diameter. Equation (C2) includes a factor of 1/3 to account for random orientation of the veins in three dimensions. As described in Sect. 4.2, we evaluate Eq. (C2) for c_B from 1 to 10 μ M, using temperature and grain size data from EDC (Fig. S1). The following parameters from Ng (2021) are used: the reference melting point $T_0 = 273.15$ K, Gibbs—Thomson coefficient $\gamma = 0.034$ J m⁻², latent heat of melting L = 333.5 J kg⁻¹, vein cross-section geometrical factor $\alpha_0 = 0.0725$, and liquidus slope $\Gamma = 4.53$ K M⁻¹ for the sulphate–H₂O system. Since empirical data for D_l below 0 °C are lacking, we approximate it with the molecular diffusivity of water by using Eq. (A1) of Ng (2023), which is valid down to –60 °C and agrees with the laboratory measurements of D_l for sulphuric acid in water from 0 to 35 °C (Umino and Newman, 1997) to within a multiplicative factor of $\approx \pm 2$.

Finally, for the "residual diffusivity" due to stochastic vein and grain-boundary motion, we use Eq. (9) of Ng (2021),

$$D_{\text{res}} = K_0 \exp(-Q/RT)/3c_1,$$
 (C3)

taking (as he did) $c_1 = 2.5$, the grain-growth rate coefficient $K_0 = 1.68 \times 10^7 \text{ mm}^2 \text{ yr}^{-1}$, activation energy $Q = 42.4 \text{ kJ mol}^{-1}$, and the gas constant $R = 8.314 \text{ J K}^{-1} \text{ mol}^{-1}$. Our models for the Gibbs–Thomson diffusion and residual diffusion encompass the two earlier grain-growth dependent models of ionic impurity diffusion by Barnes et al. (2003).